

Vertical Vortex Development in Hurricane Michael (2018) during Rapid Intensification

³ Alexander J. DesRosiers*, Michael M. Bell and Ting-Yu Cha[†]

Colorado State University, Fort Collins, Colorado

⁵ *Corresponding author address: Alexander J. DesRosiers, Department of Atmospheric Science,
⁶ Colorado State University, Fort Collins, Colorado, United States.

⁷ E-mail: adesros@rams.colostate.edu

⁸ †Current affiliation: Department of Atmospheric Science, Colorado State University, Fort Collins,
⁹ Colorado, United States.

ABSTRACT

10 The landfall of Hurricane Michael (2018) at category 5 intensity occurred
11 after rapid intensification (RI) spanning much of the storm's lifetime. Four
12 Hurricane Hunter aircraft missions observed the RI period with tail Doppler
13 radar (TDR). Data from each of the 14 aircraft passes through the storm were
14 quality controlled via a combination of interactive and machine learning tech-
15 niques. TDR data from each pass were synthesized using the SAMURAI vari-
16 ational wind retrieval technique to yield three-dimensional kinematic fields of
17 the storm to examine inner core processes during RI. Vorticity and angular
18 momentum increased and concentrated in the eyewall region. A vorticity bud-
19 get analysis indicates the tendencies became more axisymmetric over time. In
20 this study we focus in particular on how the eyewall vorticity tower builds ver-
21 tically into the upper levels. Horizontal vorticity associated with the vertical
22 gradient of tangential wind was tilted into the vertical by the eyewall updraft
23 to yield a positive vertical vorticity tendency inward atop the existing vor-
24 ticity tower, that is further developed locally upward and outward along the
25 sloped eyewall through advection and stretching. Observed maintenance of
26 thermal wind balance from a thermodynamic retrieval shows evidence of a
27 strengthening warm core, which aided in lowering surface pressure and fur-
28 ther contributed to the efficient intensification in the latter stages of this RI
29 event.

³⁰ **1. Introduction**

³¹ As large strides have been made in improving track forecasts by NOAA's National Hurricane
³² Center (NHC), intensity forecast improvements have lagged behind. Improvements have been
³³ made in intensity forecasts in recent years, but were slowest to occur in the 24 to 48-h forecast
³⁴ periods (DeMaria et al. 2014). The NHC defines rapid intensification (RI) as an increase in the
³⁵ maximum sustained winds of a tropical cyclone (TC) of at least 30 kt in a 24-h period (Kaplan
³⁶ and DeMaria 2003; Kaplan et al. 2010). More recent advancements in modeling, development of
³⁷ consensus forecast aids and RI guidance, and skill of NHC forecasters led to an increase in the
³⁸ probability of detection of short term RI events, but no notable improvement in false alarm rates
³⁹ (Cangialosi et al. 2020). From 1989-2018, RI was successfully predicted approximately 3% of the
⁴⁰ time in the Atlantic basin (Trabing and Bell 2020). Further improvements to intensity forecasting
⁴¹ depend in part on better prediction of rapid intensity changes. Poor prediction of rapid intensity
⁴² changes cause larger errors explaining roughly 20% in the yearly mean absolute errors in intensity
⁴³ forecasts over the same time period (Trabing and Bell 2020). Hendricks et al. (2010) quantified the
⁴⁴ impact of environmental factors on TC intensity change and concluded that RI is mostly controlled
⁴⁵ by internal dynamical processes in similarly favorable environments.

⁴⁶ TC intensification is a cooperative process between cloud-scale moist convection and cyclone-
⁴⁷ scale circulation that allows heat and moisture from the ocean to be utilized for TC growth and
⁴⁸ maintenance (Ooyama 1969). Increasing net vertical mass flux in the inner core due to the sec-
⁴⁹ ondary circulation composed of inflow at the surface, upward motion in the eyewall, and outflow
⁵⁰ aloft is an essential component of strengthening (Ooyama 1982). More current investigation of TC
⁵¹ intensification has placed emphasis on the mesoscale within the storm. In the beginning of the TC
⁵² life cycle, intense individual convective elements termed vortical hot towers (VHTs) pre-condition

53 the TC environment by tilting and stretching vorticity (Hendricks et al. 2004). VHTs facilitate con-
54 vergence of angular momentum in the lower levels and latent heat release as a source of warming
55 near the disturbance center. Genesis can be accomplished by the merger and axisymmetrization
56 of VHTs which can create a system-scale circulation (Montgomery et al. 2006). Discrete con-
57 vective elements remain important to the TC intensification process as it progresses towards RI.
58 Many deep convective towers locally amplify rotation in the TC at the onset of RI, but decrease
59 in number as RI proceeds (Van Sang et al. 2008). A composite study of aircraft reconnaissance
60 grouped observations in intensifying and steady state hurricanes to identify differences between
61 the groups (Rogers et al. 2013). Anomalous convective updrafts with high local vertical velocities
62 termed convective bursts (CBs) occurred with greater frequency and were preferentially located
63 within the radius of maximum wind (RMW) in the intensifying storms. Convection within the
64 RMW has been shown in theoretical work to favor RI as well (Vigh and Schubert 2009).

65 Simulation of RI indicated a synergistic relationship between CBs and the background secondary
66 circulation. Individual CBs can enhance mass flux prior to RI before the increased mass flux is
67 accomplished by the average vertical motion in the inner core (Rogers 2010). The greatest contri-
68 bution to intensification comes from the axisymmetric projection of the heating (Nolan et al. 2007)
69 which is co-located with the eyewall updraft in a TC inner core. The transition in intensification
70 from discrete CBs to a more axisymmetric secondary circulation is also hinted at in the composite
71 study of aircraft observations. Intensifying storms in the study exhibited ring-like vorticity focused
72 inside the RMW and stronger axisymmetric projections of upward motion (Rogers et al. 2013).
73 Updraft mass flux also peaked at higher altitudes and decreased less rapidly with height in the
74 intensifying storm composite observations when compared to steady state. A preference towards
75 mass flux peaks at greater elevation suggests the vertical extent of inner core eyewall convection
76 may also be important to intensification. A composite study of microwave brightness tempera-

77 tures found that during RI events a peak in 37-GHz anomalies, which are sensitive to increased
78 liquid water path from precipitation below the freezing level, preceded peaks in 85-GHz, mainly
79 due to scattering by ice water path above the freezing level (Fischer et al. 2018). The compositing
80 satellite observations lend further credence to the idea of a progression towards deeper inner core
81 convection during RI.

82 Previous studies have examined processes in the upper troposphere during RI, but there is a lack
83 of consensus on their role. Simulation of RI in Hurricane Wilma (2005) suggested the impor-
84 tance of the formation and location of the upper level warm core strengthened through subsidence
85 from deep asymmetric CBs (Chen and Zhang 2013). A double warm core structure has also been
86 simulated with the strongest warming located in the mid-level maxima (Stern and Zhang 2016).
87 Although both studies show upper level warming, with differing importance assigned to it, argu-
88 ments have been made that the height of the warm core is not related to intensity (Stern and Nolan
89 2012). However, in general warming at higher altitude in the atmosphere can be more efficient at
90 lowering surface pressure through hydrostatic arguments (Hirschberg and Fritsch 1993).

91 More detailed inner core information is required to improve skill in the prediction of RI (Ka-
92 plan et al. 2010). Research flights utilizing tail Doppler radar (TDR) have been a crucial asset
93 to furthering our understanding of inner core processes in TCs. Analysis of TDR data collected
94 during the RI of Hurricane Patricia (2015) documented an intense axisymmetric inner core which
95 extended deep into the troposphere (Rogers et al. 2017). Analysis of the axisymmetric potential
96 vorticity (PV) structure suggests that the vortex was able to concentrate PV efficiently along an-
97 gular momentum surfaces just inward of the RMW during RI over a deep layer through diabatic
98 heating (Martinez et al. 2019). Idealized numerical simulations also provide support for the idea
99 that a deeper vortex promotes faster intensification of a TC (Peng and Fang 2021).

100 Stern and Nolan (2009) used TDR data and theory to evaluate the role of vertical structure of
101 the tangential wind field in intensification of a TC, but questions remained about decay of the
102 tangential wind field in the upper levels where past observations had been more sparse. A com-
103 bination of a 14 dB increase in sensitivity (Aircraft Operations Center 2016) of the TDR flying
104 aboard the NOAA P3 Hurricane Hunter Aircraft during the 2018 Atlantic Hurricane Season and
105 the excellent aircraft data coverage during Hurricane Michael allow herein for detailed observation
106 of the upper levels during RI. The current study builds on prior work investigating the asymmetric
107 contributions to Hurricane Michael's RI deduced from radar observations (Cha et al. 2020), and
108 the relationship between sea surface temperature gradients from oceanic eddies and shear induced
109 asymmetry (Wadler et al. 2020). This study is focused on investigating the axisymmetric dynami-
110 cal aspects of vertical growth of the vorticity tower of Hurricane Michael and inferred connections
111 of upper level processes to RI of the near-surface wind field. The expansive temporal coverage
112 of aircraft observations collected by the NOAA Aircraft Operations Center provided an excellent
113 dataset with which to examine these facets of the RI process in Hurricane Michael.

114 **2. Synopsis of Hurricane Michael and observation periods**

115 The tropical depression which developed into Hurricane Michael was first designated by the
116 NHC on 0600 UTC 7 October about 130 nautical miles south of Cozumel, Mexico (Beven et al.
117 2019). The genesis occurred in a large area of disturbed weather in the Western Caribbean Sea.
118 The disturbance was composed of the remnants of Tropical Storm Kirk, a separate surface low,
119 and a larger cyclonic gyre. Moderate vertical wind shear present in the surrounding environment
120 failed to prevent intensification of the system and RI began immediately. Michael attained tropical
121 storm status 6 hours after formation and hurricane status a day later (Fig. 1a).

122 A brief pause in intensification took place on 8 October near the Western tip of Cuba as Michael
123 entered the Southern Gulf of Mexico via the Yucatan Channel. A 24-h intensification rate centered
124 on this lull is below the RI threshold which was otherwise met from designation as a tropical storm
125 onward through landfall. Reconnaissance performed by the NOAA P3 research aircraft began dur-
126 ing this time and the initial flight (yellow; Fig. 1a) sampled Michael at category 2 intensity with
127 maximum sustained winds of 85 kt. High resolution ensemble modeling of Hurricane Michael
128 initialized at 1800 UTC on 7 October found no statistical significance in structure metrics between
129 the stronger and weaker ensemble member groups 12 hours into simulation with differences in the
130 groups emerging later (Hazelton et al. 2020). These results indicate that beginning to sample the
131 storm on 8 October was well-timed to capture structural contributions to RI. Under the steering
132 influence of a ridge and mid-latitude shortwave trough, Michael took a general northward track
133 through the Gulf of Mexico. Intensification resumed on 9 October and continued until landfall.
134 Two aircraft missions (orange & blue; Fig. 1a) on 9 October captured the storm during intensifi-
135 cation from category 2 to category 4 status. A final NOAA mission (green; Fig. 1a) on 10 October
136 observed category 4 Hurricane Michael as it continued to intensify on approach to land, just before
137 the final designation of category 5 intensity near landfall. Details of the time spent in storm by the
138 P3, center fix times of passes through the storm, and their temporal position relative to the storm's
139 changing intensity are shown in Fig. 1.

140 Landfall took place at 1730 UTC 10 October near Tyndall Air Force Base in the Florida panhan-
141 dle. Minimum central pressure was recorded at 919 hPa with maximum sustained winds estimated
142 at 140 kt. Michael became the fourth storm on record to make landfall in the mainland United
143 States (US) at category 5 intensity. The storm caused extensive damage, most notably in the im-
144 mediate coastal communities of Panama City and Mexico Beach, the latter of which was impacted
145 by catastrophic storm surge reaching up to 14 feet above ground level. The storm's damaging trek

¹⁴⁶ continued inland across the Southeastern US as Michael maintained category 3 intensity while
¹⁴⁷ crossing the southwest Georgia border, making it the first major hurricane to impact the state since
¹⁴⁸ 1890 (National Weather Service 2019). The storm tracked through South Carolina, North Car-
¹⁴⁹ olina, and Virginia while undergoing extratropical transition before re-emerging over the Atlantic
¹⁵⁰ (Fig. 1b). Hurricane Michael caused \$25 billion in damage in the US and was directly responsible
¹⁵¹ for 16 deaths (Beven et al. 2019).

¹⁵² **3. Data and methodology**

¹⁵³ *a. Airborne radar data*

¹⁵⁴ Four P3 missions produced fourteen passes with adequate data coverage through the inner core.
¹⁵⁵ During each pass, the TDR employed a scan strategy which alternated between the fore and aft
¹⁵⁶ directions to produce pseudo-dual-Doppler measurements (Gamache et al. 1997). Passes were
¹⁵⁷ separated by approximately an hour with the time between center fixes not exceeding 2 hours
¹⁵⁸ except between missions. Thirty minutes of TDR data provided enough coverage to create an
¹⁵⁹ analysis of the inner core of Michael during a pass. Details of the mission durations and center fix
¹⁶⁰ times are given in Fig. 1a.

¹⁶¹ *b. Radar quality control (QC)*

¹⁶² Thorough QC efforts were necessary to remove non-weather echoes and prepare the raw TDR
¹⁶³ data for dual-Doppler analysis. Navigation errors introduced by movements of the aircraft within
¹⁶⁴ the storm and uncertainties in the inertial navigation system were corrected to obtain more accurate
¹⁶⁵ Doppler velocity and pointing angles (Cai et al. 2018). Subsequently, data from each radar scan
¹⁶⁶ were given an initial QC effort by the algorithm developed by Bell et al. (2013) that uses the
¹⁶⁷ SOLO II radar editing software from the National Center for Atmospheric Research (Oye et al.

168 1995). The algorithm is a first step to successful removal of noise, ground clutter, second trip
169 echoes, and other non-meteorological data which can prevent accurate wind synthesis from TDR
170 data. Velocity unfolding, which is necessary in a hurricane where wind speeds exceed the Nyquist
171 velocity of the TDR, is included in the algorithm. Even after automated QC, some manual effort
172 was required to produce an accurate dual-Doppler wind synthesis. Two missions, originating on
173 08 October and 10 October, received manual QC.

174 The time consuming nature of manual QC created a need to expedite the process in order to
175 analyze all available aircraft passes. A dataset composed of the post manual QC TDR scans
176 from the 3 passes during the 10 October flight was compiled to produce a random forest machine
177 learning model capable of re-creating manual QC. The technique is fully described in DesRosiers
178 (2020) and DesRosiers and Bell (2021) and briefly summarized here. After initial testing to set
179 model parameters and improve accuracy, data from the first and third passes were used to train the
180 model while withholding data from the second aircraft pass for subsequent evaluation. The model
181 was tasked with performing QC on the second pass through Hurricane Michael on 10 October
182 which it had not seen during training. A spot check for any data that should have been removed by
183 the model was performed to investigate how close the machine learning QC method could mirror
184 the already completed manual effort. Dual-Doppler analyses were produced from the data cleaned
185 by the model, data that received a subsequent spot check, and the original manual effort. All three
186 analyses were compared to determine if the method could be used to QC data from the remaining
187 two flights. The wind field obtained via machine learning QC was found to be qualitatively similar
188 to manual QC. The wind field after an additional spot check was nearly identical to manual QC.
189 Successful completion of the test allowed for the QC of remaining TDR data from both missions
190 on 9 October with the machine learning model. Additional manual checks were performed on all
191 passes that received model QC to maintain a similar standard of QC across the dataset.

192 *c. Dual Doppler analyses*

193 Dual-Doppler analyses were created for each pass with Spline Analysis at Mesoscale Utilizing
194 Radar and Aircraft Instrumentation (SAMURAI) software (Bell et al. 2012; Foerster and Bell
195 2017), which is part of the Lidar Radar Open Software Environment (LROSE; Bell (2019)). The
196 three dimensional (3D) variational data assimilation technique uses radar observations and cubic
197 b-spline basis functions to produce a best guess at the most likely state of the atmosphere by
198 minimizing a cost function. SAMURAI solves for the 3D wind field using the aforementioned
199 techniques with the addition of mass continuity as a numerical constraint. The resulting wind field
200 is represented as a 3D cubic spline function that is analytically differentiable to calculate vorticity
201 and divergence. The dual-Doppler winds were synthesized using a 1-km horizontal spline nodal
202 spacing and 0.5-km vertical nodal spacing with a $4\Delta x$ Gaussian filter in the horizontal and $2\Delta x$
203 filter in the vertical applied. With this spline nodal spacing and Gaussian filter length the minimum
204 resolved scale is ~ 4 km in the horizontal, or approximately 2.85 times the along-track data spacing
205 of ~ 1.4 km. To minimize issues from attenuation, the 2-degree beamwidth of the X-band (3-cm
206 wavelength) radar, and data coverage, the analysis was limited to the innermost 60 km of the storm.

207 Figure 2 shows reflectivity cross sections during the first and last pass of each of the four mis-
208 sions that illustrate the changes in radar presentation and organization of the storm's inner core as
209 it underwent RI in the Gulf. Cross sections are shown at 6 km to place emphasis on the increasing
210 organization in the mid-levels of the storm. Increases with time in symmetric coverage of high
211 reflectivity values denoting stronger convection are indicative of intensification. The increasing
212 symmetry is important to findings of this study and will be examined in detail. However, asym-
213 metric aspects of Hurricane Michael's evolution are also of importance and have been discussed
214 by Cha et al. (2020).

215 *d. Thermodynamic retrieval*

216 A radar-based thermodynamic retrieval technique developed for use in rapidly rotating vortices
217 (Foerster and Bell 2017; Boehm and Bell 2021) was used to discern the thermodynamic struc-
218 ture in the storm. The technique can retrieve perturbations in pressure and temperature relative
219 to a horizontally-varying reference state from the dual-Doppler winds. The thermodynamic re-
220 trieval derives pressure and temperature perturbations as three-dimensional functions using a sim-
221 ilar spline-based variational method as the SAMURAI wind retrieval. In the current study we use a
222 thermal-wind-balanced reference state which is calculated using an azimuthally averaged tangen-
223 tial wind field and the vertical temperature profile at a large radius. The moist tropical sounding
224 from Dunion (2011) was used for the outer vertical temperature profile. The sounding was chosen
225 as a time invariant climatological reference point for evaluating changes in temperature within the
226 storm as recommended by Stern and Zhang (2016). The temperature and pressure fields of the
227 reference state are obtained by integrating the thermal wind equation inward from the large radius
228 boundary. For the thermal wind calculation, the mean tangential wind is assumed constant and
229 unchanging from the 2 km vertical level to the surface due to uncertainties in the applicability of
230 gradient wind balance in the boundary layer. This assumption does not affect our conclusions as
231 our main focus in this study is on upper levels. Following the variational retrieval, we summed the
232 retrieved perturbations and reference state to obtain full three-dimensional fields of pressure and
233 density potential temperature (θ_p). We then azimuthally average the temperature similarly to the
234 wind field to produce the axisymmetric temperature field $\bar{\theta}_p$.

235 *e. Azimuthal mean calculation*

236 Axisymmetric contributions to the RI process are the primary focus of the current study. Anal-
237 yses which depict the azimuthal mean quantities as functions of radius and height are used to

238 show the evolution of Michael's structure. Each Cartesian wind analysis, performed with radial
239 resolution of 1 km and vertical resolution of 0.5 km, was re-gridded to a polar coordinate system
240 consisting of radius, azimuth, and height with azimuthal resolution of 1 degree. To prevent iso-
241 lated data points from biasing values, a 50% threshold was used as a minimum for calculating the
242 azimuthal mean. The 50% threshold was chosen based on allowable gap size in observations that
243 preserve wavenumber 0 axisymmetric structure (Lorsolo and Aksoy 2012). The gap restriction
244 allowed for calculation of the azimuthal mean quantities out to 60 km, with the innermost 40 km
245 having the best coverage from the TDR in the azimuth dimension as evidenced by the top down
246 radar reflectivity cross-sections (Fig. 2). Figures 8 and 12 are zoomed in to only 40 km radius to
247 enhance visual detail of the analysis in the eyewall region.

248 **4. Inner core changes throughout RI**

249 The availability of fourteen passes allowed for detailed documentation of the inward progression
250 of angular momentum surfaces and growth of the wind field. Absolute angular momentum (AAM)
251 is calculated using

$$252 \quad AAM = rv_t + \frac{1}{2}fr^2 \quad (1)$$

253 where f is the Coriolis force, v_t is tangential wind, and r is radius from storm center. The pro-
254 gression of the $1.0 \times 10^6 \text{ m}^2 \text{ s}^{-1}$ AAM contour during each pass is shown in Fig. 3a. The surface
255 moved radially inward and became increasingly vertically aligned at higher altitudes with time.

256 The evolving tangential wind field is shown in Fig. 3b by tracking the changes in the hurricane
257 force (33 m s^{-1}) wind contour. The contour outline became broader and deeper in response to an
258 increase in the area of hurricane force winds in the vortex. As RI proceeded, hurricane force winds
extended further radially outward from the center and increased in depth through the troposphere.

259 *a. Changes in angular momentum and vorticity*

260 Angular momentum and vertical vorticity changes during each of the four aircraft missions were
261 calculated by a point subtraction method normalized to hourly tendencies by taking the difference
262 between the center fix times of the first to last pass in hours. Changes in AAM (ΔM) are calculated
263 by:

$$\Delta M = (AAM_{Last} - AAM_{First}) / (t_{Last} - t_{First}) \quad (2)$$

264 at each radius and height between the first and last center fixes of an aircraft mission. Flights took
265 approximately 2-5 hours between the first and last center fix of each depending on the amount of
266 time spent in storm by the P3 (Fig. 1a). Figure 4 shows the calculated changes in AAM in color
267 with contours of the AAM surfaces during the final pass in each panel to illustrate the resulting
268 structure after changes. AAM changes during mission 1008H1 in Fig. 4a are rather modest and
269 not well organized with negative magnitudes observed in the eyewall. The weak AAM change is
270 likely related to both the brief pause in intensification (Fig. 1a) and the prevalence of asymmetries
271 at this time (Fig. 7a,b,c) which may not project well onto an azimuthal average. Sharp gradients
272 in the AAM surfaces are indicative of the eyewall location. Over the following three missions,
273 increases in ΔM concentrate mainly in the eyewall region with peak magnitudes in the mid-levels
274 during the two missions in Figs. 4b and 4c. A weaker peak positive magnitude is observed in the
275 final mission which extends through the bulk of the eyewall region with peak hourly rates of gain
276 in excess of $0.1 \times 10^6 \text{ m}^2 \text{ s}^{-1}$ near 8 km altitude. Consistent positive ΔM values were observed
277 in the upper troposphere during all missions. ΔM values during the final 3 missions are mainly
278 positive, indicating larger values of AAM moving radially inward throughout the inner core of
279 Hurricane Michael.

280 Vertical vorticity (ζ) changes are determined by the same point subtraction method used for ΔM :

$$\Delta\zeta = (\zeta_{Last} - \zeta_{First}) / (t_{Last} - t_{First}) \quad (3)$$

281 The magnitudes of $\Delta\zeta$ per hour, shown in color in Fig. 5, increase with time throughout intensifi-
282 cation with the exception of a more modest increase mostly below hourly gains of $50 \times 10^{-5} \text{ s}^{-1}$
283 observed during mission 1009H2 (Fig. 5c). Contours of absolute vorticity observed during the last
284 pass of each mission show the structure present after changes during each mission. The non-linear
285 rates with which internal organization and magnitude of vertical vorticity increase are apparent
286 when tracking changes through each mission. The main region of positive $\Delta\zeta$ began as a broad
287 outward tilted area and became more focused in the eyewall region with time. Large magnitudes
288 of positive $\Delta\zeta$ in excess of $50 \times 10^{-5} \text{ s}^{-1}$ per hour first concentrate in the middle to upper levels in
289 Fig. 5b during 1009H1. In Figs. 5c and 5d positive $\Delta\zeta$ begins to concentrate at all levels through-
290 out the eyewall region with a slight lapse in the mid-levels during mission 1009H2 (Figure 5c). A
291 well defined signal for vorticity gain was present during 1010H1 with peak magnitudes over 100
292 $\times 10^{-5} \text{ s}^{-1}$ per hour in lower and upper levels (Fig. 5d). During mission 1010H1, a strong dipole
293 in $\Delta\zeta$ develops with negative values appearing around 20 km radius.

294 The axisymmetric tangential wind field from the last 7 passes through Hurricane Michael is
295 shown in Fig. 6, during which time a consistent vertical development of the inner core was ob-
296 served. Maximum azimuthally averaged values of tangential wind increased at an approximate
297 pace of 1 m s^{-1} per hour over the course of these last two missions and increased in depth through-
298 out the troposphere. The RMW became more vertical and contracted inward. A radially inward
299 jump in RMW at 1 km altitude in one pass was likely due to issues of P-3 flight path affecting radar
300 geometry and was corrected (Fig. 6a). The expansion of tangential wind values upward during
301 the final pass (Fig. 6g) shows that wind speeds within 6 m s^{-1} of the peak azimuthally averaged

302 value (66 m s^{-1}) are found up to roughly 7 km. As the tangential wind field strengthened and
303 grew in depth, the region where the vertical gradient was maximized became located at increasing
304 heights in the vortex. The importance of this vertical gradient of tangential wind to the RI process
305 is discussed in the following section.

306 **5. Axisymmetric vertical development of the vorticity tower**

307 The latter two aircraft missions into Hurricane Michael prior to landfall documented a part of the
308 RI event characterized by consistent vertical development of the eyewall vorticity tower into the
309 upper levels. The novel and detailed look of how RI takes place in the upper levels gives a unique
310 opportunity to diagnose mechanisms that may have been responsible. Axisymmetric dynamics
311 played a large role in intensification during the latter two missions and a vorticity budget approach
312 was used to identify the increasingly axisymmetric nature of Hurricane Michael's RI. Thermody-
313 namics were also at play in the vertical expansion taking place atop the eyewall. The impacts of
314 both dynamics and thermodynamics on storm structure are considered to evolve together as the
315 temporal gap between observations is too great to determine if one leads the other.

316 *a. Increasing symmetry of RI*

317 Existing TC intensification theories focus on both axisymmetric and asymmetric modes. Studies
318 that focus on the axisymmetric mode often build on the Sawyer-Eliassen equation (Eliassen 1951)
319 to explain symmetric intensification in a framework termed the balanced vortex model. In the
320 model, a forced secondary circulation comprised of lower level inflow, updrafts and latent heating
321 near the center, and outflow aloft, becomes stronger and drives intensification (Vigh and Schubert
322 2009). The rotating convection paradigm seeks to explain intensification through an asymmetric
323 process. The framework emphasizes localized rotating convective updrafts in the eyewall of a TC

324 which enhance organization and structure of the storm's inner core (Montgomery 2016). Both the-
 325 ories are critical to understanding TC intensification, however they vary on the point of symmetry
 326 in the vortex and intensification mechanism. A cylindrical coordinate vorticity budget equation
 327 (Reasor et al. 2009) was used to examine the evolution of the symmetry of intensification during
 328 Hurricane Michael's RI:

$$\begin{aligned}
 \frac{\partial_L}{\partial t} \bar{\zeta} = & -\bar{u} \frac{\partial \bar{\zeta}}{\partial r} - \bar{w} \frac{\partial \bar{\zeta}}{\partial z} - (f_0 + \bar{\zeta}) \bar{\delta} - \overline{\frac{\partial \bar{w}}{\partial r} \frac{\partial \bar{v}}{\partial z}} \\
 & - \left[\bar{u}' \frac{\partial \zeta'}{\partial r} + \frac{\bar{v}' \partial \zeta'}{\partial \lambda} \right] - \overline{\bar{w}' \frac{\partial \zeta'}{\partial z}} - \bar{\zeta}' \bar{\delta}' - \left[\overline{\frac{\partial w'}{\partial r} \frac{\partial v'}{\partial z}} + \frac{1}{r} \overline{\frac{\partial w'}{\partial \lambda} \frac{\partial u'}{\partial z}} \right]
 \end{aligned} \quad (4)$$

329 where prime terms denote eddy, or asymmetric, contributions that vary azimuthally, an overbar
 330 indicates an azimuthal average of the quantity, $\frac{\partial_L}{\partial t}$ is the local time tendency, δ is divergence, f_0 is
 331 the Coriolis parameter, and λ indicates the azimuthal dimension in cylindrical coordinates. Con-
 332 fidence in the exact partitioning of vorticity tendency between the axisymmetric and asymmetric
 333 components is lowered by the temporal resolution of the analyses, but the budget approach is use-
 334 ful for examining changes in symmetry throughout the whole of the observed RI event. The first
 335 line of Eq. 4 is composed of four terms which quantify the vertical vorticity tendencies associ-
 336 ated with (1) axisymmetric radial advection, (2) vertical advection, (3) stretching, and (4) tilting
 337 of horizontal vorticity. A summation of these first four terms gives a total axisymmetric vortic-
 338 ity tendency at the time of an aircraft pass. The second line of the equation is made up of four
 339 terms (5-8) corresponding to the same aforementioned tendencies but instead as asymmetric eddy
 340 contributions. Terms 5 and 8 (in brackets) are composed of two expressions. Summing these
 341 second line terms yields a total asymmetric vorticity tendency. A sum of all terms in the budget
 342 produces a total vorticity tendency for both symmetric and asymmetric contributions at the time
 343 of the analysis.

344 Figure 7 shows the three summation values of asymmetric, axisymmetric, and total tendencies.
345 Confidence in tendency values within the eye at smaller radii is low due to potential numerical
346 instability as radius goes to zero in the calculation of Eq. 4. A single pass from each mission
347 was chosen to illustrate the RI process as it proceeded from a mainly asymmetric to mainly ax-
348 isymmetric mode. The increased symmetry is most evident in the passes from the first and last
349 missions. Figures 7a and 7c are nearly identical as asymmetric vorticity tendency terms dominated
350 the changes occurring on 8 October. Figures 7k and 7l are nearly identical on 10 October when
351 axisymmetric tendency terms dominated. The increasing axisymmetry and decreasing asymmetry
352 with time is further confirmed by a Pearson correlation calculation for each pass shown in Fig. 7.
353 The variance explained (r^2) by the asymmetric and axisymmetric tendencies to the total tendency
354 shows that asymmetric intensification was more dominant early on but axisymmetric intensifica-
355 tion became a more appropriate conceptual model in the later stages of RI. These results are con-
356 sistent with tangential wind momentum budget analysis of modeled fields of Hurricane Michael
357 where mean transport terms dominated the net tangential wind spin-up in later RI as compared to
358 eddy terms in early RI (Green et al. 2021). In the following section we focus on the latter period
359 where axisymmetric dynamics dominate in order to further investigate the growth of the vorticity
360 tower during RI.

361 *b. Dynamical impacts*

362 Persistent spatial patterns were identified in the vorticity budget tendencies during the latter half
363 of Michael's observed RI. Here we focus on 1230 UTC on 10 October when the axisymmetric
364 tendencies were greatest prior to landfall. Figure 8 shows the calculated axisymmetric vorticity
365 tendency terms from the final aircraft pass, with contours overlaid showing the total summation of
366 all tendency terms in the budget including asymmetries. As shown in Fig. 7j-l, the total vorticity

367 tendency observed was dominated by axisymmetric terms at this time. The radial advection (Fig.
368 8a) and vertical advection (Fig. 8b) have oppositely signed, sloped tripole patterns maximized
369 in the upper troposphere. Similarly, stretching (Fig. 8c) and tilting (Fig. 8d) largely oppose each
370 other in an upper-tropospheric tripole pattern, with the negative stretching tendency having a larger
371 magnitude in the lower troposphere. Qualitatively, the radial advection and stretching tendencies
372 have similar spatial patterns, and their sum can be considered as the radial flux divergence of
373 vorticity. Both the vertical advection and tilting tendencies also have similarities, and their sum
374 can be considered as the vertical flux divergence of vorticity. While all 4 terms are important,
375 we argue here that the vertical development of the tower into the upper levels of the troposphere
376 was accomplished through re-orientation of horizontal vorticity into the vertical and the transport
377 of existing vertical vorticity upward by the positive vertical velocity in the eyewall. The strong
378 positive tilting tendency on the inner edge of the eyewall is associated with the interaction of the
379 vertical gradient of tangential wind and radial gradient of vertical velocity. However only a small
380 portion of the large tilting tendency was located in a net positive total tendency region, as much
381 of it was offset by negative stretching tendency associated with upper-level divergence. While the
382 tilting and vertical advection are positively associated with the updraft and upward development,
383 we interpret the stretching and radial advection as acting together to primarily build the tower
384 outward in the upper levels. The eyewall slope, which is greater in the upper than lower levels, is
385 expected based on the majority of cases analyzed sharing this characteristic in observations using
386 airborne radar in Atlantic TCs (Hazelton and Hart 2013). The tripole pattern acts to redistribute
387 vorticity radially inward and outward, but the magnitude of the positive tendencies is much weaker
388 in the eye. The primary effect of the combined stretching and radial advection in the upper levels
389 of the vorticity tower is therefore a dipole tendency that moves vorticity radially outward towards

390 the RMW. The net effect of all tendency terms shown creates a positive total tendency (contoured)
391 slightly radially inward of the RMW.

392 To investigate the upward development of the vorticity tower, Fig. 9 shows the azimuthally
393 averaged evolution of the horizontal and vertical vorticity over four aircraft passes from 1009H2
394 when the contribution that tilting made to storm development first became clear. In a warm-
395 cored TC, tangential wind decays with height which generates horizontal vorticity, mathematically
396 defined as the negative of the vertical gradient of the tangential wind component, or $-\frac{\partial v}{\partial z}$. The
397 intersection of the axisymmetric updraft, shown in the secondary circulation vectors in the top
398 row of Fig. 9, along with the horizontal vorticity shown in color, created axisymmetric tilting
399 tendency terms in the vorticity budget (Eq. 4). The tendency was positive on the radially inward
400 edge of the updraft and negative on the outer edge. The regions of positive tendency, shown
401 in warm colors in the middle row, are areas of the storm where the horizontal vorticity was re-
402 oriented into the vertical vorticity with cyclonic rotation. There is also an accompanying negative
403 dipole that produces vertical vorticity with anticyclonic rotation. The dipole structure between the
404 two tendencies became more noticeable during the latter passes of 1009H2 in Figs. 9g and 9h.
405 Vertical vorticity in the eyewall (Figs. 9i-l) showed increased magnitude where the positive tilting
406 tendencies occur progressively higher in the storm. The same behavior continued with greater
407 magnitude during the flight into Michael on 10 October prior to landfall (Fig. 10). Figure 10i
408 shows the final observed axisymmetric vorticity tower prior to landfall exhibiting coherent and
409 nearly uniform structure from the surface to approximately 12 km.

410 *c. Thermodynamical impacts*

411 In addition to dynamical impacts, we seek to investigate the role of thermodynamic factors in
412 Hurricane Michael's RI using the observations. The radar-based thermodynamic retrieval tech-

413 nique described in the methodology section 3d (Foerster and Bell 2017) was applied to the winds
414 during the final 2 aircraft missions (1009H2 & 1010H1). Here we focus on the retrieved density
415 potential temperature to assess the evolution of the TC warm-core.

416 The dynamics and thermodynamics are closely coupled via thermal wind balance as described
417 by the following relationship:

$$\hat{f} \frac{\partial v}{\partial \tilde{z}} = \frac{g}{\theta_{\rho,0}} \left(\frac{\partial \theta_{\rho}}{\partial r} \right)_{\tilde{z}} \quad (5)$$

418 Equation 5 is in pseudo-height coordinates (Hoskins and Bretherton 1972; Schubert and Hack
419 1982; Schubert et al. 2017) where $\hat{f} = f + \frac{2v}{r}$, \tilde{z} is pseudo-height, g is gravity, and $\theta_{\rho,0}$ is a refer-
420 ence density potential temperature. We show the pseudo-height relationship here since it directly
421 illustrates the specific thermodynamic quantity retrieved in our analysis $\bar{\theta}_{\rho}$. We note that the re-
422 trieval temperature from the observations shown here is the sum of retrieved perturbations and
423 the reference state, and therefore does not explicitly assume thermal wind balance holds. Thermo-
424 dynamic fields shown were not interpolated from height to pseudo-height coordinates for a direct
425 assessment of thermal-wind balance, but rather we use the above equation to gain insight into the
426 mechanisms by which dynamic and thermodynamic mechanisms work together during RI.

427 During 1009H2 & 1010H1, negative vertical gradients of tangential wind (left side of Eq. 5)
428 were present in the upper levels of the eyewall, shown as positive horizontal vorticity in Figs. 9
429 and 10. If the vortex is in approximate thermal wind balance, the areas with positive horizontal
430 vorticity should be associated with negative radial gradients of density potential temperature (right
431 side of Eq. 5). Figure 11 shows the retrieved density potential temperature and its radial gradient
432 during the last two missions. The dynamics of these last two missions were analyzed in Figs. 6,
433 9, and 10. The lowest 2 km was excluded from this analysis given the aforementioned constraints
434 of the thermodynamic retrieval method in lowest levels of the storm. The presence of the warm
435 core was assessed by taking the $\bar{\theta}_{\rho}$ field in the inner core and subtracting the averaged profile at

436 $r = 60$ km. The warm core temperature anomaly increased in magnitude in the upper levels with
437 time, consistent with the increasing intensity and decreasing surface pressure. Increases in $\left(\frac{\partial \theta_p}{\partial r}\right)$
438 shown as contours in Fig. 11 were co-located with areas of stronger horizontal vorticity during the
439 later stages of intensification (cf. Figs. 9 and 10). Increasing warm core temperature anomalies
440 and areas where tilting was maximized were coincident with respect to height, providing a link
441 between dynamic and thermodynamic impacts via the thermal wind equation. Small biases in
442 warm core temperature anomaly arise from the choice of sounding reference profile (not shown),
443 but the conclusions are not sensitive to the sounding used in the retrieval.

444 The cumulative picture gleaned from the analyses is that the storm continuously tilted horizontal
445 vorticity into the vertical at increasing heights via the eyewall updraft, coupled simultaneously
446 with the maintenance of thermal wind balance and changes to the radial gradient of temperature
447 and an increasing warm core temperature anomaly. The co-location of tilting tendencies and the
448 increasingly negative gradient of $\bar{\theta}_p$ provides observational evidence of the interconnected nature
449 of the dynamic and thermodynamic processes that contributed to the vertical growth of the vorticity
450 tower in Hurricane Michael.

451 6. Discussion

452 The intensification of a TC via tilting of horizontal vorticity has been examined in other contexts.
453 In cyclogenesis, convective bursts tilt ambient low-level horizontal vorticity into the vertical while
454 also stretching the vertical vorticity due to low-level convergence (Montgomery et al. 2006). In
455 contrast to that conceptual model, the upper-level process of tilting and stretching in Michael's RI
456 was due to axisymmetric features that allowed tilting to be a persistent upper-level process rather
457 than an episodic low-level one. Additionally, the advection and stretching terms take on a different
458 role here compared to the genesis stage, as is discussed further below.

459 Some similarities to the conceptual model described here can be seen in the secondary eyewall
460 development of Hurricane Rita (2005), where a positive vorticity tilting tendency occurred radially
461 inward of the secondary eyewall (Didlake and Houze Jr. 2011). Structure differentiates the Rita
462 case from the one analyzed in Michael. The reflectivity and associated convection of the forming
463 secondary eyewall in Rita was less uniform by visual inspection than the axisymmetric convective
464 ring observed in the mature inner eyewall of Hurricane Michael. Another difference appears to be
465 that the updraft in the secondary eyewall of Rita was centered in the reflectivity tower, while the
466 updraft in Michael's eyewall was displaced slightly radially outward of the center of the reflectivity
467 tower in the sloped eyewall. This difference results in co-location of the positive tilting tendency
468 with the top of the existing vorticity tower. We hypothesize that the specific location of the eyewall
469 updraft and slope of both the updraft and vorticity tower played an important role in Michael's RI.
470 Further research is needed to determine whether this hypothesis can generalize to other RI cases.

471 While we have emphasized tilting herein, it was only part of the observed inner core dynamics.
472 The dipole nature of tilting prevents the term from increasing the net circulation on its own. The
473 negative tilting portion of the dipole is located near strong upper level outflow shown by secondary
474 circulation vectors (Figure 9d) which can advect the negative vorticity out of the inner core. The
475 positive tilting tendency is on the inner edge of the updraft where vertical advection can transport
476 the re-orientated horizontal vorticity and pre-existing vertical vorticity upward to build the tower
477 in the vertical. Radial advection and stretching were shown to further redistribute and concentrate
478 the vorticity outward along the sloped eyewall towards the RMW where the vorticity tower is
479 maximized and reinforced.

480 The total positive vorticity tendency resulting from all axisymmetric terms was located along
481 the inner edge of the RMW where convective heating, evidenced by the updraft, took place.
482 Convective heating in the eyewall causes thermally indirect subsidence warming inside the eye

(Willoughby 1998). Towards the end of the observation period of Michael, accompanying down-drafts on the inner edge of the upper eyewall, shown by secondary circulation vectors (Figs. 9 and 10), were observed indicators of subsidence. Resulting forced dry descent as a consequence of heating in the eyewall aids in making the eye cloud free (Houze Jr. 2010), which was observed via satellite imagery (not shown) showing a clearing eye during the final two missions. The descent leads to continued strengthening of the warm core. Additionally, diabatic heating from eyewall convection itself will also contribute to the warm core, with increasing efficiency of heating as a vortex gets stronger (Schubert and Hack 1982; Nolan et al. 2007). Finer points of structure, location, and intensity of the warm core could not be speculated on without more concrete thermodynamic observations available above aircraft reconnaissance flight level. However, a growing warm core temperature perturbation was consistent with ongoing dynamic processes via thermal wind balance where tilting and the radial gradient of $\bar{\theta}_p$ were maximized in the upper levels. This warming in the upper levels must impact near-surface intensification of the vortex through hydrostatic balance. In the stratospheric level of insignificant dynamics (LID) assumption, which is valid on TC scales, local temperature changes at any level above the surface and below the LID contribute to the pressure tendency at the surface (Hirschberg and Fritsch 1993). Furthermore, warming in the upper levels where density is lower and there is greater spacing between isobars has a greater impact on the surface pressure than warming at lower levels would. Lower surface pressure correlates with intensification of the wind field in the lower troposphere due to a greater pressure gradient force.

Although the axisymmetric vorticity tower became more thinly concentrated in physical space, the angular momentum surfaces moved radially inward faster than the convective heating and the updraft. A comparison of the tracked AAM surface in Fig. 3a to the secondary circulation vectors (Figs. 9 and 10) support the inward movement of angular momentum surfaces outpacing

507 the heating. As a result, the dynamic size of heating increased along with the efficiency of heating
508 when considered in the potential radius framework pioneered by Schubert and Hack (1983). As
509 the eyewall remained fixed to the inside edge of the RMW, it still moved inward towards the storm
510 center as the RMW contracted (Fig. 7), a behavior also linked to increased subsidence in the
511 eye (Willoughby 1998). While we have focused here on vorticity and its tendencies from tilting,
512 stretching, and advection, the relationship between heating and intensification is more succinct in
513 a potential vorticity framework. Further analysis of Michael's RI from a complementary potential
514 vorticity perspective (Martinez et al. 2019) is warranted.

515 Lastly, we note that tendency terms in the vorticity budget indicated intensification was mainly
516 axisymmetric in the later stages of RI, but eddy contributions were non-negligible. The genera-
517 tion of polygonal eyewalls and eye-eyewall mixing in TCs has been long established in theo-
518 retical frameworks and observation (Kossin and Eastin 2001; Schubert et al. 1999). More recent
519 work simulating RI in Typhoon Megi (2010) credit mesovortices at polygonal eyewall vertices as
520 agents of intensification via localized increases in radial AAM advection and heat fluxes within
521 the RMW (Lee and Wu 2018). Polygonal eyewall structure was observed in Hurricane Michael
522 as it approached the Florida coast (Cha et al. 2020), but analysis of these features and their role is
523 beyond the scope of the current study.

524 7. Conclusion

525 Four missions flown by the NOAA Hurricane Hunters provided an opportunity to investigate
526 Hurricane Michael's historic RI event in the Gulf of Mexico which led to the fourth recorded
527 landfall of a category 5 hurricane in the United States. Fourteen aircraft passes through the storm
528 allowed for snapshots of the evolution in the inner core of the storm. Point subtractions between
529 analyses at the start and end of each aircraft mission quantified changes in vertical vorticity and

530 angular momentum. Changes in both quantities exhibited increasingly positive magnitudes which
531 concentrated in the eyewall region as the RI event progressed. Angular momentum changes were
532 largely positive while the vorticity changes progressed towards a dipole with positive magnitude
533 changes in the vorticity tower and negatives just radially outside. Inward movement of angular
534 momentum surfaces and growth of the hurricane force wind field were documented. An analy-
535 sis of the contributions of asymmetric and symmetric vorticity tendencies show that the vortex
536 intensification progressed towards axisymmetry with greater efficiency over time.

537 Temporal coverage of Hurricane Michael during RI allowed for observation of the vortex as it
538 built vertically into the upper levels of the troposphere. The mechanisms that led to this vertical
539 development discussed in this study are illustrated schematically in Fig. 12. Tilting of the ambient
540 horizontal vorticity, created by the decay of the tangential wind field with height, by the eyewall
541 updraft was found to create a dipole tendency with the positive tendency inward atop the existing
542 vorticity tower and the negative tendency radially outward of the updraft in a region of outflow.
543 Tilting has been identified as an intensification mechanism in other stages of the TC life cycle, but
544 the detailed observations of this process atop the eyewall of a rapidly intensifying Atlantic hurri-
545 cane provide a novel look at its importance at upper-levels during RI. Tilting alone cannot increase
546 the overall circulation within the inner core, and the growth of the vortex tower required contribu-
547 tions from advection and stretching as well. Vertical advection transported vertical vorticity from
548 the tower upward, including that re-oriented by tilting, while stretching and radial advection acted
549 to move the vorticity outward and amplify the vorticity along the inner edge of the RMW.

550 A thermodynamic retrieval technique provided evidence of the maintenance of thermal wind
551 balance and an increasing warm core temperature perturbation in the upper levels where heat-
552 ing can have an increased impact on surface pressure. The co-location of the radial gradient of
553 density potential temperature and tilting tendency show the interconnected nature of the dynamic

554 and thermodynamic mechanisms of intensification. Warming in the upper levels has a more sub-
555 stantial impact than warming closer to the surface on lowering the minimum sea level pressure.
556 Connections between tilting, diabatic heating, and eye subsidence that enhance the warm core can
557 therefore lower surface pressure, allowing mechanisms of RI taking place in the upper levels to
558 play a role in the intensification of the near-surface wind field. Hurricane Michael's well-defined
559 axisymmetric structure shown in these analyses suggest the mechanisms explored in this study
560 took place in a nearly continuous and efficient manner. The co-location of the sloped eyewall
561 updraft, vertical vorticity tower, and horizontal vorticity made available for tilting by the decaying
562 winds aloft were able to produce rapid surface pressure falls in Hurricane Michael. However, it
563 is still unclear if this specific arrangement of heating and structure is a universal pathway to ver-
564 tical development in RI cases. It is evident from the analyses herein that producing a stronger
565 TC requires producing a deeper vortex. Further investigation of the intensification mechanisms
566 presented here through both future observations and modeling studies is recommended. Improved
567 understanding of inner core processes which allow storms to undergo RI should aid in improving
568 short term intensity forecasts in the future.

569 *Acknowledgments.* This research was financially supported National Science Foundation award
570 OAC-1661663 and Office of Naval Research awards N000141613033 and N000142012069. We
571 would like to thank NOAA Aircraft Operations Center and the Hurricane Research Division of the
572 Atlantic Oceanographic and Meteorological Laboratory for collecting the airborne tail Doppler
573 radar data used for this study. We also thank Rachel Mauk and two anonymous reviewers for
574 comments and suggestions which improved the manuscript.

575 *Data Availability Statement*

576 The dataset analyzed from Hurricane Michael in this study can be found online at
577 <https://doi.org/10.5281/zenodo.5146325>.

578 **References**

- 579 Aircraft Operations Center, 2016: Tropical cyclone operations: Challenges in 2015; New prod-
580 ucts and services planned for 2016 and 2017. NOAA Office of Marine and Aviation Opera-
581 tions, cited: 2020-09-29, [Available online at <https://www.ofcm.gov/meetings/TCORF/ihc16/2016presentations.html>].
- 583 Bell, M. M., 2019: nsf-lrose/lrose-blaze: lrose-blaze-20190105. doi:10.5281/ZENODO.2532758,
584 URL <https://doi.org/10.5281/zenodo.2532758#.XebvCW0eoLk.mendeley>.
- 585 Bell, M. M., W.-C. Lee, C. A. Wolff, and H. Cai, 2013: A Solo-based automated quality control
586 algorithm for airborne tail Doppler radar data. *J. Appl. Meteor. Climatol.*, **52**, 2509–2528, doi:
587 10.1175/JAMC-D-12-0283.1.
- 588 Bell, M. M., M. T. Montgomery, and K. A. Emanuel, 2012: Air–sea enthalpy and momentum
589 exchange at major hurricane wind speeds observed during CBLAST. *J. Atmos. Sci.*, **69**, 3197–
590 3222, doi:doi.org/10.1175/JAS-D-11-0276.1.
- 591 Beven, J. L., R. Berg, and A. Hagen, 2019: National Hurricane Center tropical cyclone report:
592 Hurricane Michael (AL142018). NHC Tech. Rep.
- 593 Boehm, A. M., and M. M. Bell, 2021: Retrieved thermodynamic structure of Hurricane Rita
594 (2005) from airborne multi-Doppler radar data. *J. Atmos. Sci.*, doi:10.1175/JAS-D-20-0195.1.

- 595 Cai, H., W.-C. Lee, M. M. Bell, C. A. Wolff, X. Tang, and F. Roux, 2018: A generalized navigation
596 correction method for airborne Doppler radar data. *J. Atmos. Oceanic Technol.*, **35**, 1999–2017,
597 doi:10.1175/JTECH-D-18-0028.1.
- 598 Cangialosi, J. P., E. Blake, M. DeMaria, A. Penny, A. Latto, E. Rappaport, and V. Tallapragada,
599 2020: Recent progress in tropical cyclone intensity forecasting at the National Hurricane Center.
600 *Wea. Forecasting*, **35**, 1913–1922, doi:10.1175/WAF-D-20-0059.1.
- 601 Cha, T.-Y., M. M. Bell, W.-C. Lee, and A. J. DesRosiers, 2020: Polygonal eyewall asymme-
602 tries during the rapid intensification of Hurricane Michael (2018). *Geophys. Res. Lett.*, **47**,
603 e2020GL087919, doi:10.1029/2020GL087919.
- 604 Chen, H., and D.-L. Zhang, 2013: On the rapid intensification of Hurricane Wilma (2005). Part
605 II: Convective bursts and the upper-level warm core. *J. Atmos. Sci.*, **70**, 146–162, doi:10.1175/
606 JAS-D-12-062.1.
- 607 DeMaria, M., C. R. Sampson, J. A. Knaff, and K. D. Musgrave, 2014: Is tropical cyclone intensity
608 guidance improving? *Bull. Amer. Meteor. Soc.*, **95**, 387–398, doi:10.1175/BAMS-D-12-00240.
609 1.
- 610 DesRosiers, A. J., 2020: Airborne radar quality control and analysis of the rapid intensification
611 of Hurricane Michael (2018). M.S. thesis, Department of Atmospheric Science, Colorado State
612 University.
- 613 DesRosiers, A. J., and M. M. Bell, 2021: Airborne radar quality control with machine learning.
614 **Submitted.**
- 615 Didlake, A. C., and R. A. Houze Jr., 2011: Kinematics of the secondary eyewall observed in
616 Hurricane Rita (2005). *J. Atmos. Sci.*, **68**, 1620–1636, doi:10.1175/2011JAS3715.1.

- 617 Dunion, J. P., 2011: Rewriting the climatology of the tropical North Atlantic and Caribbean Sea
atmosphere. *J. Climate*, **24** (3), 893–908, doi:10.1175/2010JCLI3496.1.
- 618
- 619 Eliassen, A., 1951: Slow thermally or frictionally controlled meridional circulation in a circular
620 vortex. *Astrophysica Norvegica*, **5**, 19–60.
- 621
- 622 Fischer, M. S., B. H. Tang, K. L. Corbosiero, and C. M. Rozoff, 2018: Normalized convective
623 characteristics of tropical cyclone rapid intensification events in the North Atlantic and Eastern
624 North Pacific. *Mon. Wea. Rev.*, **146**, 1133–1155, doi:10.1175/MWR-D-17-0239.1.
- 625
- 626 Foerster, A. M., and M. M. Bell, 2017: Thermodynamic retrieval in rapidly rotating vortices from
multiple-Doppler radar data. *J. Atmos. Oceanic Technol.*, **34** (11), 2353–2374, doi:10.1175/
JTECH-D-17-0073.1.
- 627
- 628 Gamache, J. F., J. S. Griffin, P. P. Dodge, and N. F. Griffin, 1997: Evaluation of a fully three-
dimensional variational Doppler analysis technique, preprints, 28th Conf. on Radar Meteorology,
629 Austin, TX, Amer. Meter. Soc.
- 630
- 631 Green, A., S. G. Gopalakrishnan, G. J. Alaka Jr., and S. Chia, 2021: Understanding the role of
mean and eddy momentum transport in the rapid intensification of Hurricane Irma (2017) and
632 Hurricane Michael (2018). *Atmosphere*, **12**, 492, doi:10.3390/atmos12040492.
- 633
- 634 Hazelton, A. T., and R. E. Hart, 2013: Hurricane eyewall slope as determined from airborne radar
reflectivity data: Composites and case studies. *Wea. Forecasting*, **28**, 368–386, doi:10.1175/
WAF-D-12-00037.1.
- 635
- 636 Hazelton, A. T., X. Zhang, S. Gopalakrishnan, W. Ramstrom, F. Marks, and J. A. Zhang, 2020:
637 High-resolution ensemble HFV3 forecasts of Hurricane Michael (2018): Rapid intensification
638 in shear. *Mon. Wea. Rev.*, **148** (5), 2009–2032, doi:10.1175/MWR-D-19-0275.1.

- 639 Hendricks, E. A., M. T. Montgomery, and C. A. Davis, 2004: The role of “vortical” hot towers in
640 the formation of Tropical Cyclone Diana (1984). *J. Atmos. Sci.*, **61**, 1209–1232, doi:10.1175/
641 1520-0469(2004)061<1209:TROVHT>2.0.CO;2.
- 642 Hendricks, E. A., M. S. Peng, B. Fu, and T. Li, 2010: Quantifying environmental control on tropi-
643 cal cyclone intensity change. *Mon. Wea. Rev.*, **138**, 3243–3271, doi:10.1175/2010MWR3185.1.
- 644 Hirschberg, P. A., and J. M. Fritsch, 1993: On understanding height tendency. *Mon. Wea. Rev.*,
645 **121**, 2646–2661, doi:10.1175/1520-0493(1993)121<2646:OUHT>2.0.CO;2.
- 646 Hoskins, B. J., and F. P. Bretherton, 1972: Atmospheric frontogenesis models: Mathematical
647 formulation and solution. *J. Atmos. Sci.*, **29** (1), 11–37, doi:10.1175/1520-0469(1972)029<0011:
648 AFMMFA>2.0.CO;2.
- 649 Houze Jr., R. A., 2010: Clouds in tropical cyclones. *Mon. Wea. Rev.*, **138**, 293–344, doi:10.1175/
650 2009MWR2989a.1.
- 651 Kaplan, J., and M. DeMaria, 2003: Large-scale characteristics of rapidly intensifying trop-
652 ical cyclones in the North Atlantic basin. *Wea. Forecasting*, **18**, 1093–1108, doi:10.1175/
653 1520-0434(2003)018<1093:LCORIT>2.0.CO;2.
- 654 Kaplan, J., M. DeMaria, and J. A. Knaff, 2010: A revised tropical cyclone rapid intensification
655 index for the Atlantic and Eastern North Pacific basins. *Wea. Forecasting*, **25**, 220–241, doi:
656 10.1175/2009WAF2222280.1.
- 657 Kossin, J. P., and M. D. Eastin, 2001: Two distinct regimes in the kinematic and thermo-
658 dynamic structure of the hurricane eye and eyewall. *J. Atmos. Sci.*, **58**, 1079–1090, doi:
659 10.1175/1520-0469(2001)058<1079:TDRITK>2.0.CO;2.

- 660 Lee, J.-D., and C.-C. Wu, 2018: The role of polygonal eyewalls in rapid intensification of Typhoon
661 Megi. *J. Atmos. Sci.*, **75**, 4175–4199, doi:10.1175/JAS-D-18-0100.1.
- 662 Lorsolo, S., and A. Aksoy, 2012: Wavenumber analysis of azimuthally distributed data:
663 Assessing maximum allowable gap size. *Mon. Wea. Rev.*, **140**, 1945–1956, doi:10.1175/
664 MWR-D-11-00219.1.
- 665 Martinez, J., M. M. Bell, R. Rogers, and J. D. Doyle, 2019: Axisymmetric potential vorticity evo-
666 lution of Hurricane Patricia (2015). *J. Atmos. Sci.*, **76**, 2043–2063, doi:10.1175/JAS-D-18-0373.
667 1.
- 668 Montgomery, M. T., 2016: Introduction to hurricane dynamics: Tropical cyclone intensification.
669 *Advanced Numerical Modeling and Data Assimilation Techniques for Tropical Cyclone Pre-*
670 *diction*, U. C. Mohanty, and S. G. Gopalakrishnan, Eds., Springer, Dordrecht., chap. 21-22,
671 537–559.
- 672 Montgomery, M. T., M. E. Nicholls, T. A. Cram, and A. B. Saunders, 2006: A vortical hot tower
673 route to tropical cyclogenesis. *J. Atmos. Sci.*, **63**, 355–386, doi:10.1175/JAS3604.1.
- 674 National Weather Service, 2019: Hurricane Michael hits Georgia. NOAA, URL https://www.weather.gov/ffc/2018_hurricane_michael.
- 675
- 676 Nolan, D. S., Y. Moon, and D. P. Stern, 2007: Tropical cyclone intensification from asymmetric
677 convection: Energetics and efficiency. *J. Atmos. Sci.*, **64**, 3377–3405, doi:10.1175/JAS3988.1.
- 678 Ooyama, K. V., 1969: Numerical simulation of the life cycle of tropical cyclones. *J. Atmos. Sci.*,
679 **26**, 3–40, doi:10.1175/1520-0469(1969)026<0003:NSOTLC>2.0.CO;2.
- 680 Ooyama, K. V., 1982: Conceptual evolution of the theory and modeling of the tropical cyclone. *J.*
681 *Meteor. Soc. Japan*, **60**, 369–380, doi:10.2151/jmsj1965.60.1_369.

- 682 Oye, R., C. Mueller, and S. Smith, 1995: Software for radar translation, visualization, editing, and
683 interpolation, preprints, 27th Conf. on Radar Meteorology, Vail, CO, Amer. Meter. Soc.
- 684 Peng, K., and J. Fang, 2021: Effect of the initial vortex vertical structure on early development of
685 an axisymmetric tropical cyclone. *J. Geophys. Res.*, **126**, doi:10.1029/2020JD033697.
- 686 Reasor, P. D., M. D. Eastin, and J. F. Gamache, 2009: Rapidly intensifying Hurricane Guillermo
687 (1997). Part I: Low-wavenumber structure and evolution. *Mon. Wea. Rev.*, **137**, 603–631, doi:
688 10.1175/2008MWR2487.1.
- 689 Rogers, R., 2010: Convective-scale structure and evolution during a high-resolution simulation of
690 tropical cyclone rapid intensification. *J. Atmos. Sci.*, **67**, 44–70, doi:10.1175/2009JAS3122.1.
- 691 Rogers, R., P. Reasor, and S. Lorsolo, 2013: Airborne Doppler observations of the inner-core
692 structural differences between intensifying and steady-state tropical cyclones. *Mon. Wea. Rev.*,
693 **141**, 2970–2991, doi:10.1175/MWR-D-12-00357.1.
- 694 Rogers, R. F., and Coauthors, 2017: Rewriting the tropical record books: The extraordinary
695 intensification of Hurricane Patricia (2015). *Bull. Amer. Meteor. Soc.*, **98**, 2091–2112, doi:
696 10.1175/BAMS-D-16-0039.1.
- 697 Schubert, W. H., S. R. Fulton, and P. E. Ciesielski, 2017: Elliptic transverse circulation equations
698 for balanced models in a generalized vertical coordinate. *arXiv preprint arXiv:1705.05460*.
- 699 Schubert, W. H., and J. J. Hack, 1982: Inertial stability and tropical cyclone development. *J.*
700 *Atmos. Sci.*, **39** (8), 1687–1697, doi:10.1175/1520-0469(1982)039<1687:ISATCD>2.0.CO;2.
- 701 Schubert, W. H., and J. J. Hack, 1983: Transformed Eliassen balanced vortex model. *J. Atmos.*
702 *Sci.*, **40**, 1571–1583, doi:10.1175/1520-0469(1983)040<1571:TEBVM>2.0.CO;2.

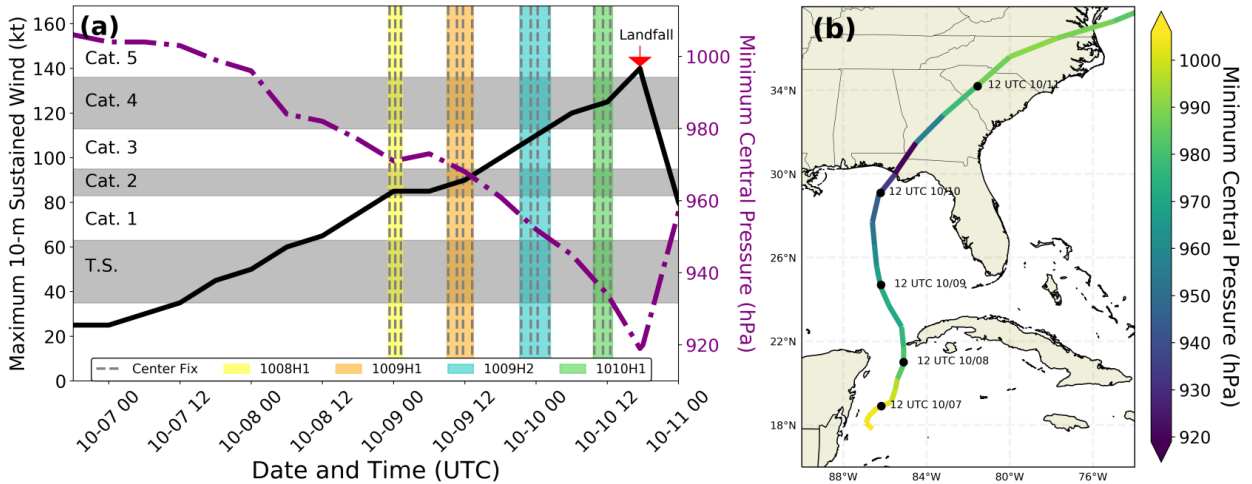
- 703 Schubert, W. H., M. T. Montgomery, R. K. Taft, T. A. Guinn, S. R. Fulton, J. P. Kossin, and
704 J. P. Edwards, 1999: Polygonal eyewalls, asymmetric eye contraction, and potential vorticity
705 mixing in hurricanes. *J. Atmos. Sci.*, **56**, 1197–1223, doi:10.1175/1520-0469(1999)056<1197:
706 PEAECA>2.0.CO;2.
- 707 Stern, D. P., and D. S. Nolan, 2009: Reexamining the vertical structure of tangential winds
708 in tropical cyclones: Observations and theory. *J. Atmos. Sci.*, **66**, 3579–3600, doi:10.1175/
709 2009JAS2916.1.
- 710 Stern, D. P., and D. S. Nolan, 2012: On the height of the warm core in tropical cyclones. *J. Atmos.*
711 *Sci.*, **69**, 1657–1680, doi:10.1175/JAS-D-11-010.1.
- 712 Stern, D. P., and F. Zhang, 2016: The warm-core structure of Hurricane Earl (2010). *J. Atmos. Sci.*,
713 **73**, 3305–3328, doi:10.1175/JAS-D-15-0328.1.
- 714 Trabing, B. C., and M. M. Bell, 2020: Understanding error distributions of hurricane intensity
715 forecasts during rapid intensity changes. *Wea. Forecasting*, **35** (6), 2219–2234, doi:10.1175/
716 WAF-D-19-0253.1.
- 717 Van Sang, N., R. K. Smith, and M. T. Montgomery, 2008: Tropical-cyclone intensification and
718 predictability in three dimensions. *Quart. J. Roy. Meteor. Soc.*, **137**, 563–582, doi:10.1002/qj.
719 235.
- 720 Vigh, J. A., and W. H. Schubert, 2009: Rapid development of the tropical cyclone warm core. *J.*
721 *Atmos. Sci.*, **66**, 3335–3350, doi:10.1175/2008MWR2487.1.
- 722 Wadler, J. B., J. A. Zhang, R. F. Rogers, B. Jaimes, and L. K. Shay, 2020: The rapid intensification
723 of Hurricane Michael (2018): Storm structure and the relationship to environmental and air-sea
724 interactions. *Mon. Wea. Rev.*, **149**, 245–267, doi:10.1175/MWR-D-20-0145.1.

- ₇₂₅ Willoughby, H. E., 1998: Tropical cyclone eye thermodynamics. *Mon. Wea. Rev.*, **126**, 3053–3067,
- ₇₂₆ doi:10.1175/1520-0493(1998)126<3053:TCET>2.0.CO;2.

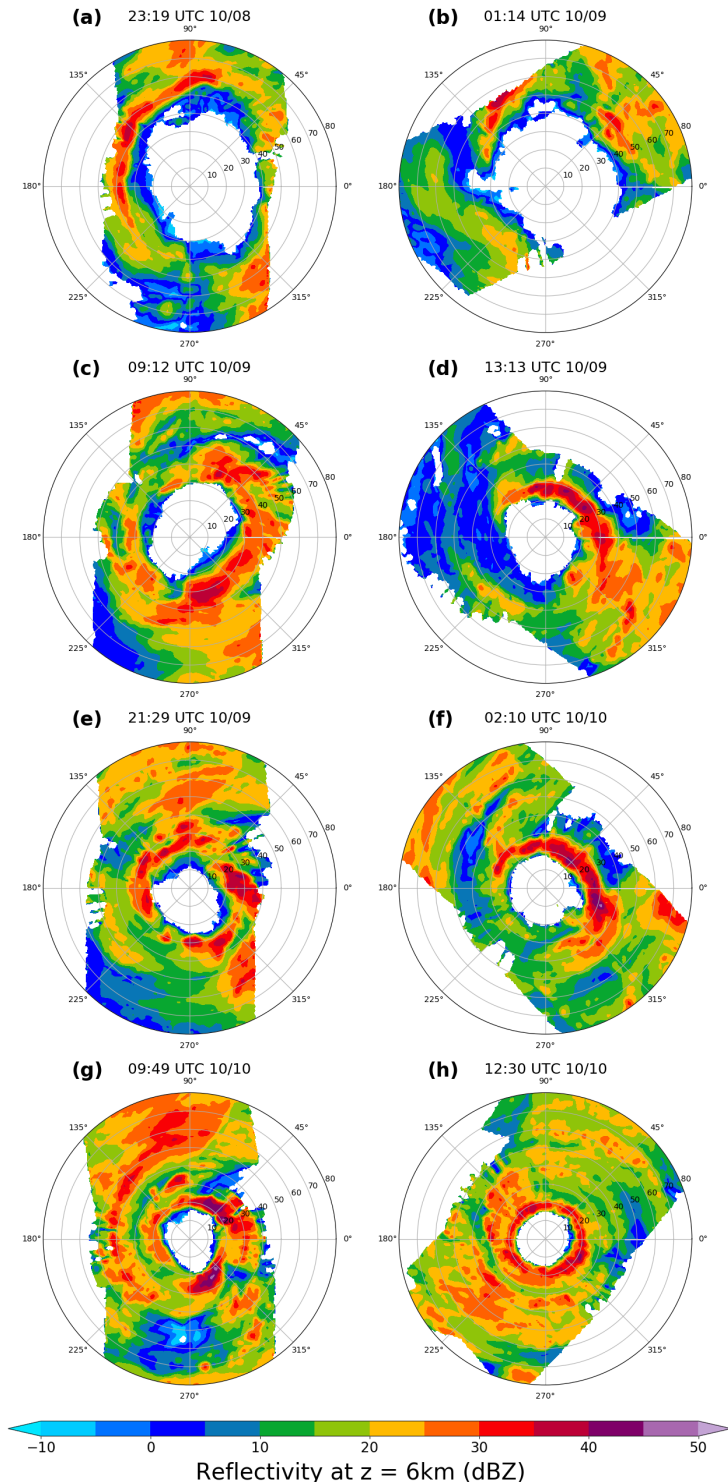
727 LIST OF FIGURES

728	Fig. 1. NHC Best Track maximum sustained 10 meter wind speed (kt) and minimum central pressure (hPa) from genesis through shortly after landfall (a). Observation periods by the P3 research aircraft are highlighted with embedded dashed lines indicating the time at which the aircraft reached the center during each pass through Hurricane Michael. Track of the storm from genesis through exit from the United States with minimum central pressure shaded (b).	37
730		
731		
732		
733	Fig. 2. Polar plots of radar reflectivity at 6 km altitude. The first and last aircraft pass from 1008H1(a,b), 1009H1 (c,d), 1009H2 (e,f), and 1010H1 (g,h) are shown with center fix times displayed at the top of each panel.	38
734		
735		
736	Fig. 3. Progression of the azimuthally averaged $1 \times 10^6 \text{ m}^2 \text{ s}^{-1}$ absolute angular momentum (AAM) contour and b) hurricane force 33 m s^{-1} wind contour during each of the fourteen aircraft passes.	39
737		
738		
739	Fig. 4. ΔM per hour shaded in color from the first to the last center fix of each aircraft mission. Differences are calculated in $10^6 \text{ m}^2 \text{ s}^{-1} \text{ h}^{-1}$ during (a) 1008H1, (b) 1009H1, (c) 1009H2, and (d) 1010H1. Positive values show increases in M over time. Contours show the AAM ($10^6 \text{ m}^2 \text{ s}^{-1}$) structure at the time of the final fix.	40
740		
741		
742		
743	Fig. 5. $\Delta \zeta$ per hour shaded in color from the first to the last center fix of each aircraft mission. Differences are calculated in $10^{-5} \text{ s}^{-1} \text{ h}^{-1}$ during (a) 1008H1, (b) 1009H1, (c) 1009H2, and (d) 1010H1. Positive values show increases in absolute vertical vorticity over time. Contours show the vorticity (10^{-5} s^{-1}) structure at the time of the final fix.	41
744		
745		
746		
747	Fig. 6. Progression of the azimuthally averaged tangential wind field (color, m s^{-1}) during the last two aircraft missions, 1009H2 (a,b,c,d) and 1010H1 (e,f,g), prior to landfall. The radius of maximum wind is denoted in black. Analysis times are listed above each panel.	42
748		
749		
750	Fig. 7. Vorticity budget tendency terms from the asymmetric (left column) and symmetric (middle column) contributions to Hurricane Michael's total vorticity tendency (right column) over time. The four passes are approximately 12 hours apart with center fix times shown to the left of each row. A representative pass was chosen from the (a,b,c) 1008H1, (d,e,f) 1009H1, (g,h,i) 1009H2, and (j,k,l) 1010H1 aircraft missions. The radius of maximum wind is shown in black. Variance explained (r^2) of the total tendency by the asymmetric and axisymmetric tendency is shown in the top right of the panels.	43
751		
752		
753		
754		
755		
756		
757	Fig. 8. Axisymmetric vorticity budget tendency terms for (a) radial advection, (b) vertical advection, (c) stretching, and (d) tilting during the final pass through Hurricane Michael prior to landfall at 12:30 UTC on 10 October 2018. The summation of all instantaneous tendency terms including asymmetric terms is contoured (also shown in Fig. 7l). The radius of maximum wind is denoted in white. Secondary circulation vectors are given in gray.	44
758		
759		
760		
761		
762	Fig. 9. Azimuthally averaged horizontal vorticity (color, 10^{-5} s^{-1}) with secondary circulation vectors (top row), axisymmetric tilting tendency of vorticity ($\text{s}^{-1} \text{ h}^{-1}$, middle row) and vertical vorticity (10^{-5} s^{-1} , bottom row). Analysis is from aircraft passes at 21:29 UTC (a,e,i) and 23:07 UTC (b,f,j) on 09 October and 00:15 UTC (c,g,k) and 02:10 UTC (d,h,l) on 10 October during aircraft mission 1009H2.	45
763		
764		
765		
766		
767	Fig. 10. As in Figure 9 but from aircraft passes at 09:49 UTC (a,d,g), 11:17 UTC (b,e,h), and 12:30 UTC (c,f,i) on 10 October during aircraft mission 1010H1.	46
768		

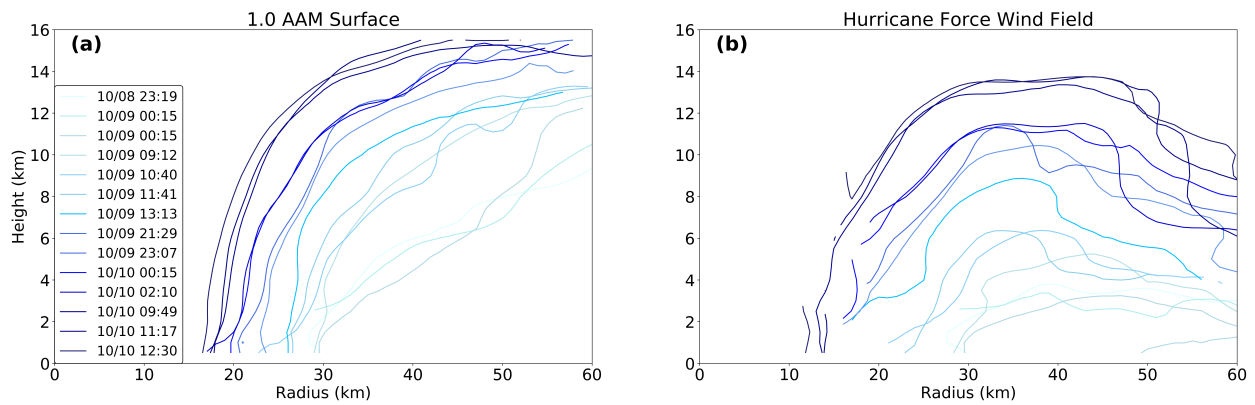
Fig. 12. Schematic representation of observed vortex development processes during rapid intensification of Hurricane Michael (2018). Light gray shading denotes the eyewall cloud. Purple shaded region represents the tower of high vorticity in the eyewall. Green shading denotes region of positive vorticity tendency from tilting and vertical advection. Blue shading represents region of positive vorticity tendency from stretching and radial advection. The + sign denotes the location of the maximized positive net vertical vorticity tendency from the sum of these terms and negative tendencies (not shown). Yellow shading denotes secondary circulation. Cyan contour denotes the radius of maximum wind. Dashed gray contours denote tangential wind, with decreasing line thickness indicating weaker winds. The region of enhanced horizontal vorticity is denoted near 9 km altitude at the same level as the red shaded area where warm core development is maximized through thermal wind balance.



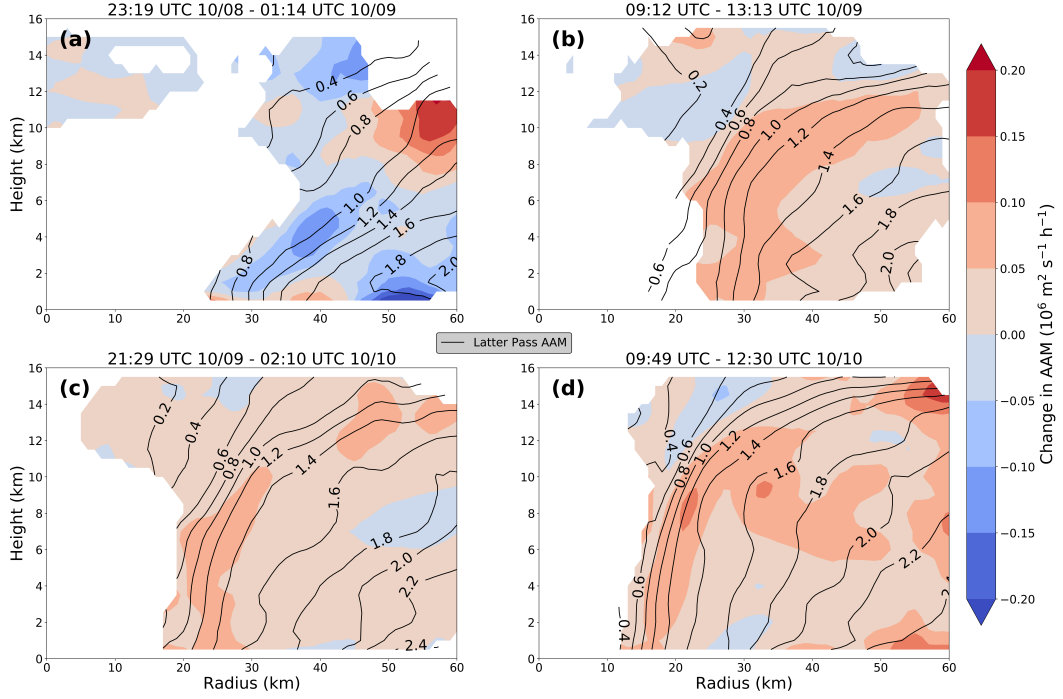
785 FIG. 1. NHC Best Track maximum sustained 10 meter wind speed (kt) and minimum central pressure (hPa)
 786 from genesis through shortly after landfall (a). Observation periods by the P3 research aircraft are highlighted
 787 with embedded dashed lines indicating the time at which the aircraft reached the center during each pass through
 788 Hurricane Michael. Track of the storm from genesis through exit from the United States with minimum central
 789 pressure shaded (b).



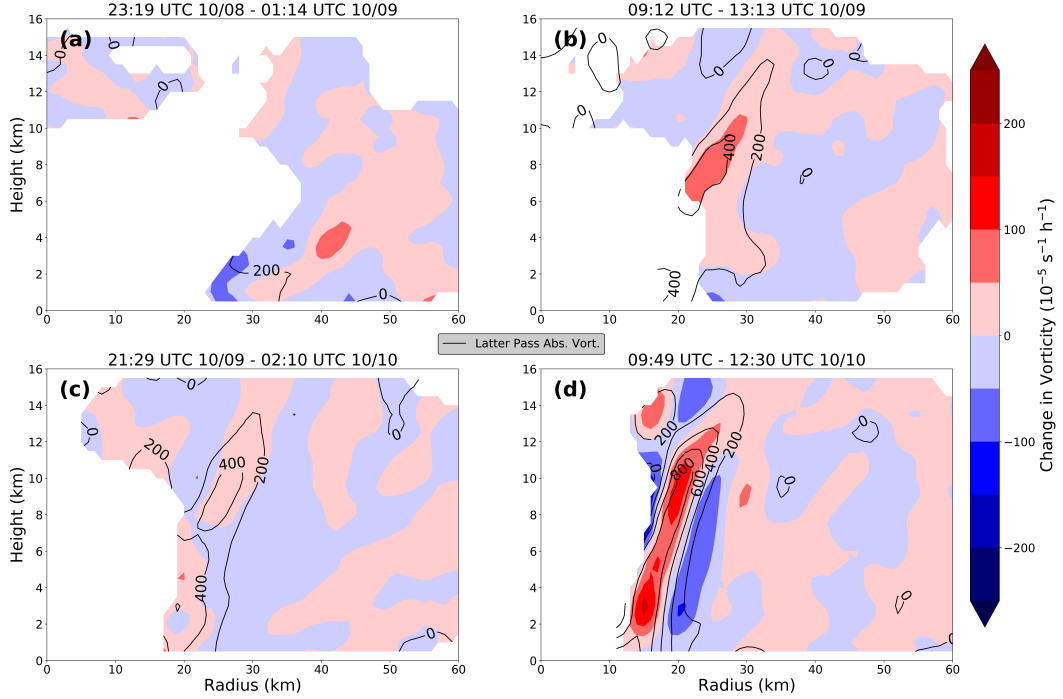
790 FIG. 2. Polar plots of radar reflectivity at 6 km altitude. The first and last aircraft pass from 1008H1(a,b),
 791 1009H1 (c,d), 1009H2 (e,f), and 1010H1 (g,h) are shown with center fix times displayed at the top of each panel.



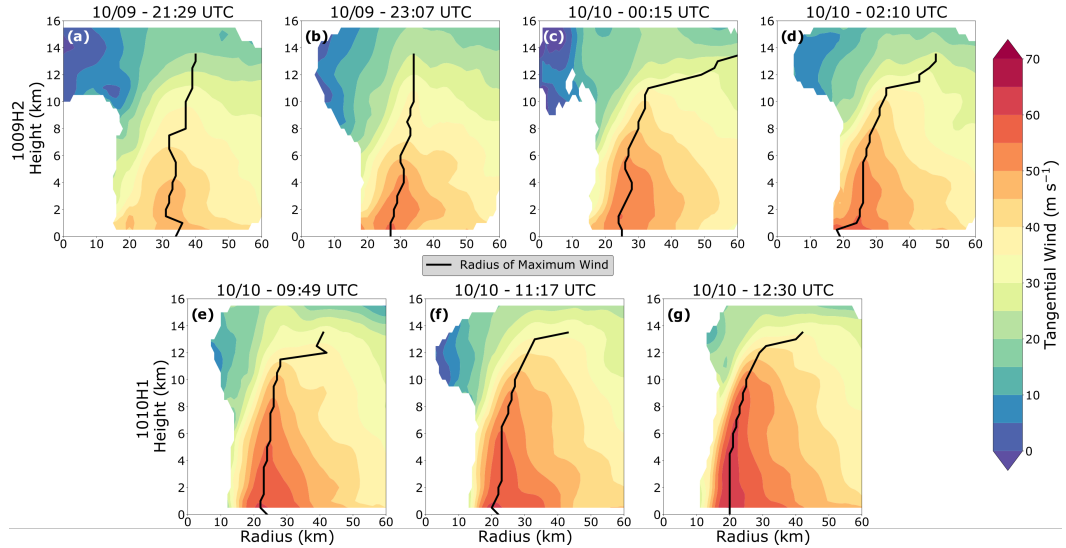
792 FIG. 3. Progression of the azimuthally averaged $1 \times 10^6 \text{ m}^2 \text{ s}^{-1}$ absolute angular momentum (AAM) contour
 793 and b) hurricane force 33 m s^{-1} wind contour during each of the fourteen aircraft passes.



794 FIG. 4. ΔM per hour shaded in color from the first to the last center fix of each aircraft mission. Differences
 795 are calculated in $10^6 \text{ m}^2 \text{ s}^{-1} \text{ h}^{-1}$ during (a) 1008H1, (b) 1009H1, (c) 1009H2, and (d) 1010H1. Positive values
 796 show increases in M over time. Contours show the AAM ($10^6 \text{ m}^2 \text{s}^{-1}$) structure at the time of the final fix.

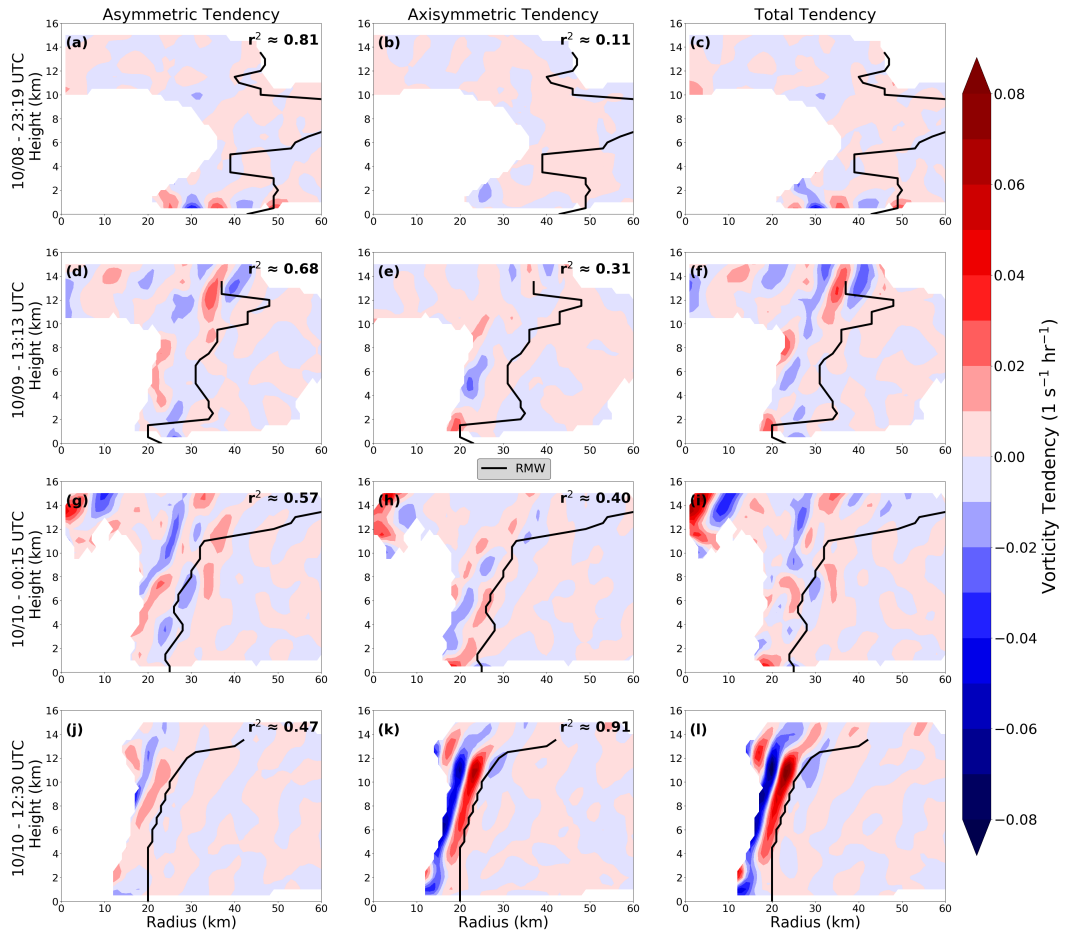


797 FIG. 5. $\Delta\zeta$ per hour shaded in color from the first to the last center fix of each aircraft mission. Differences
 798 are calculated in $10^{-5} \text{ s}^{-1}\text{h}^{-1}$ during (a) 1008H1, (b) 1009H1, (c) 1009H2, and (d) 1010H1. Positive values
 799 show increases in absolute vertical vorticity over time. Contours show the vorticity (10^{-5} s^{-1}) structure at the
 800 time of the final fix.

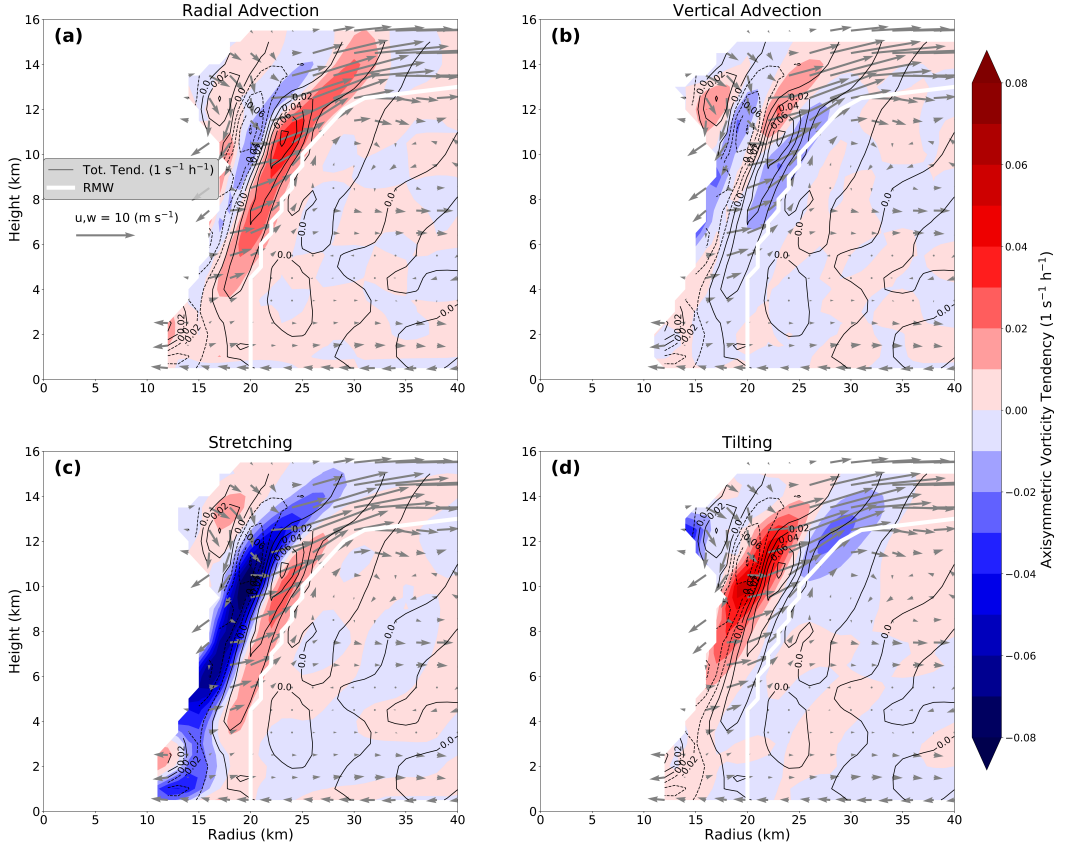


801 FIG. 6. Progression of the azimuthally averaged tangential wind field (color, m s^{-1}) during the last two aircraft
 802 missions, 1009H2 (a,b,c,d) and 1010H1 (e,f,g), prior to landfall. The radius of maximum wind is denoted in
 803 black. Analysis times are listed above each panel.

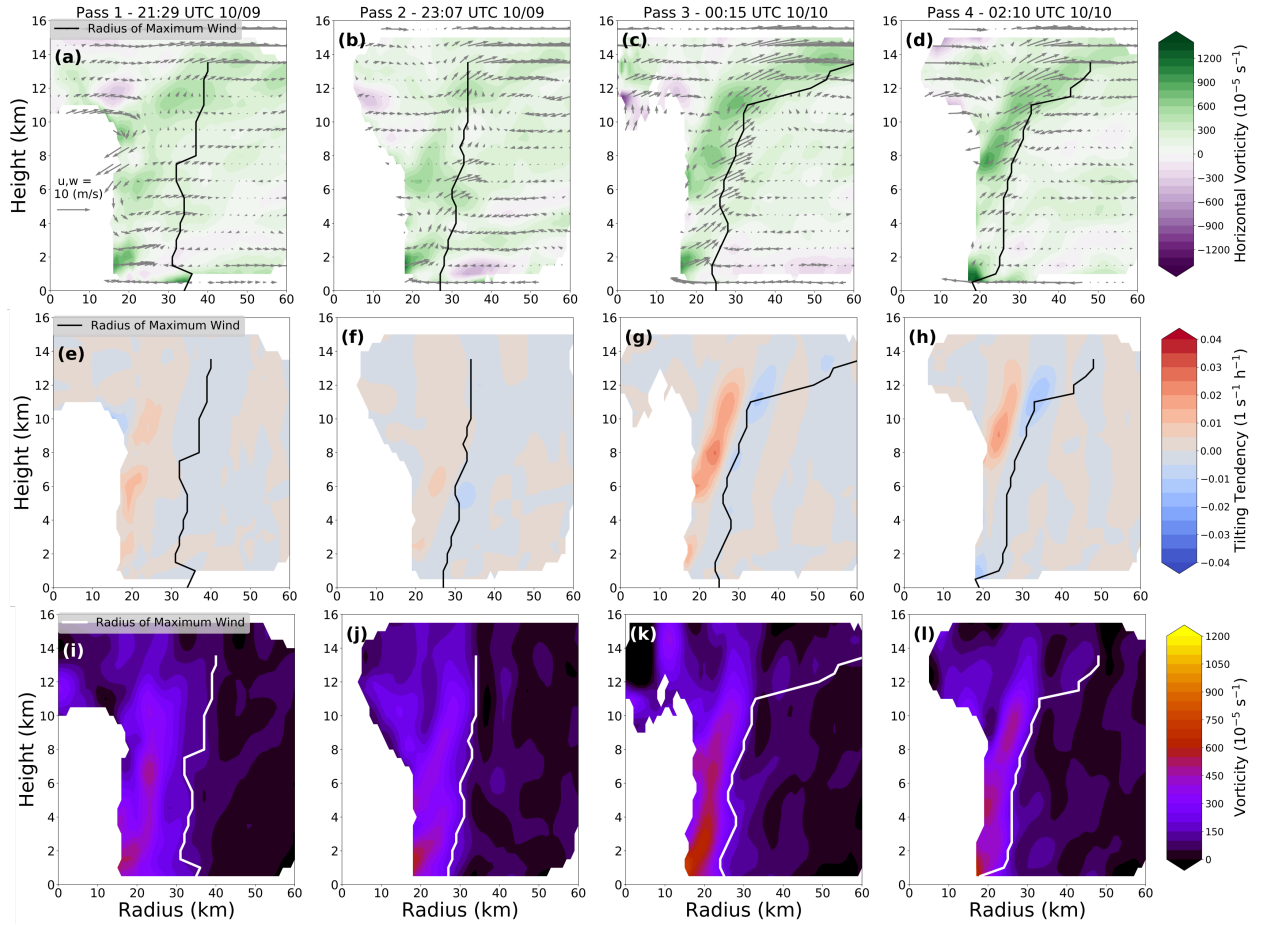
804
 811
 817
 822
 825



805 FIG. 7. Vorticity budget tendency terms from the asymmetric (left column)
806 contributions to Hurricane Michael's total vorticity tendency (right column) over time. The four passes are
807 approximately 12 hours apart with center fix times shown to the left of each row. A representative pass was
808 chosen from the (a,b,c) 1008H1, (d,e,f) 1009H1, (g,h,i) 1009H2, and (j,k,l) 1010H1 aircraft missions. The
809 radius of maximum wind is shown in black. Variance explained (r^2) of the total tendency by the asymmetric and
810 axisymmetric tendency is shown in the top right of the panels.



812 FIG. 8. Axisymmetric vorticity budget tendency terms for (a) radial advection, (b) vertical advection, (c)
813 stretching, and (d) tilting during the final pass through Hurricane Michael prior to landfall at 12:30 UTC on 10
814 October 2018. The summation of all instantaneous tendency terms including asymmetric terms is contoured
815 (also shown in Fig. 7l). The radius of maximum wind is denoted in white. Secondary circulation vectors are
816 given in gray.



818 FIG. 9. Azimuthally averaged horizontal vorticity (color, 10^{-5} s^{-1}) with secondary circulation vectors (top
 819 row), axisymmetric tilting tendency of vorticity ($\text{s}^{-1} \text{ h}^{-1}$, middle row) and vertical vorticity (10^{-5} s^{-1} , bottom
 820 row). Analysis is from aircraft passes at 21:29 UTC (a,e,i) and 23:07 UTC (b,f,j) on 09 October and 00:15 UTC
 821 (c,g,k) and 02:10 UTC (d,h,l) on 10 October during aircraft mission 1009H2.

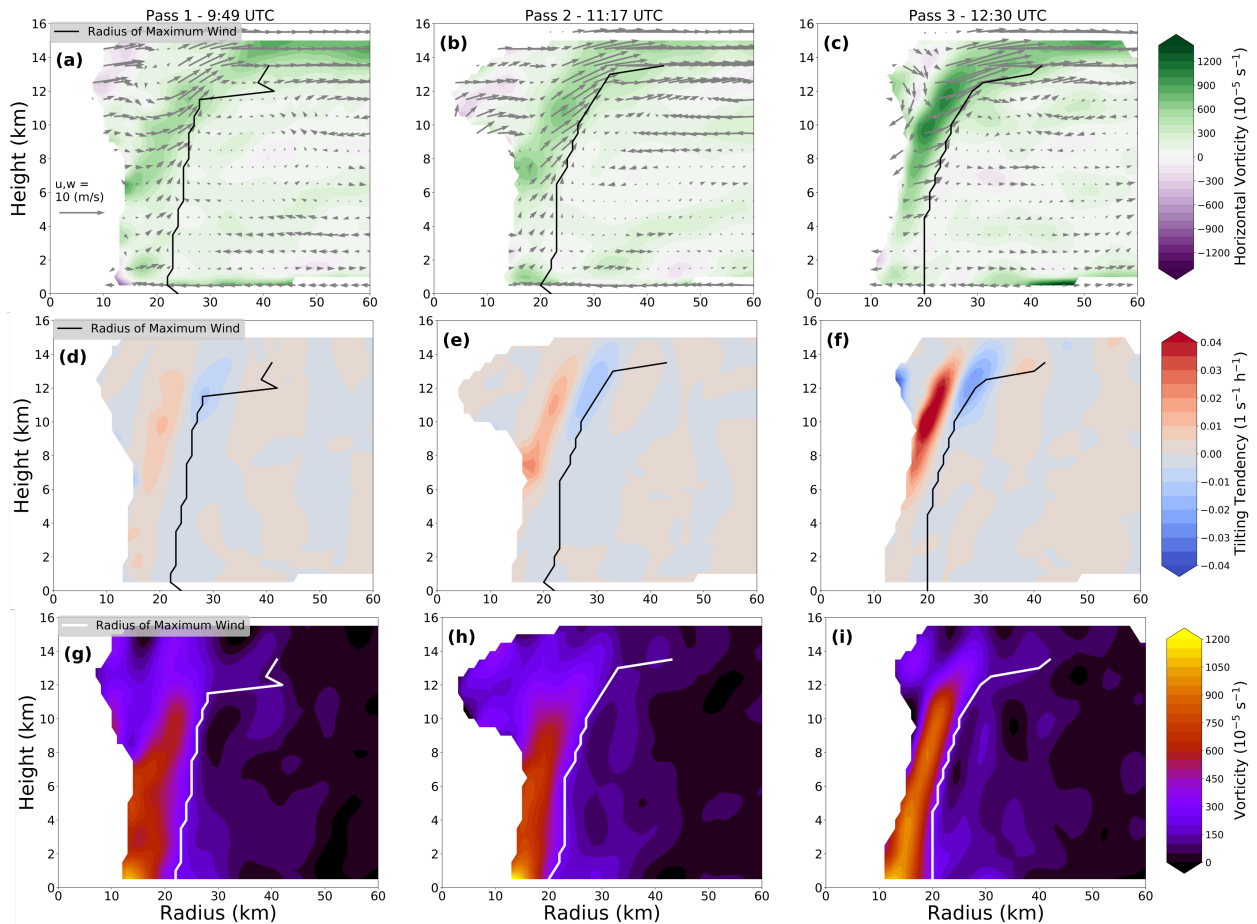
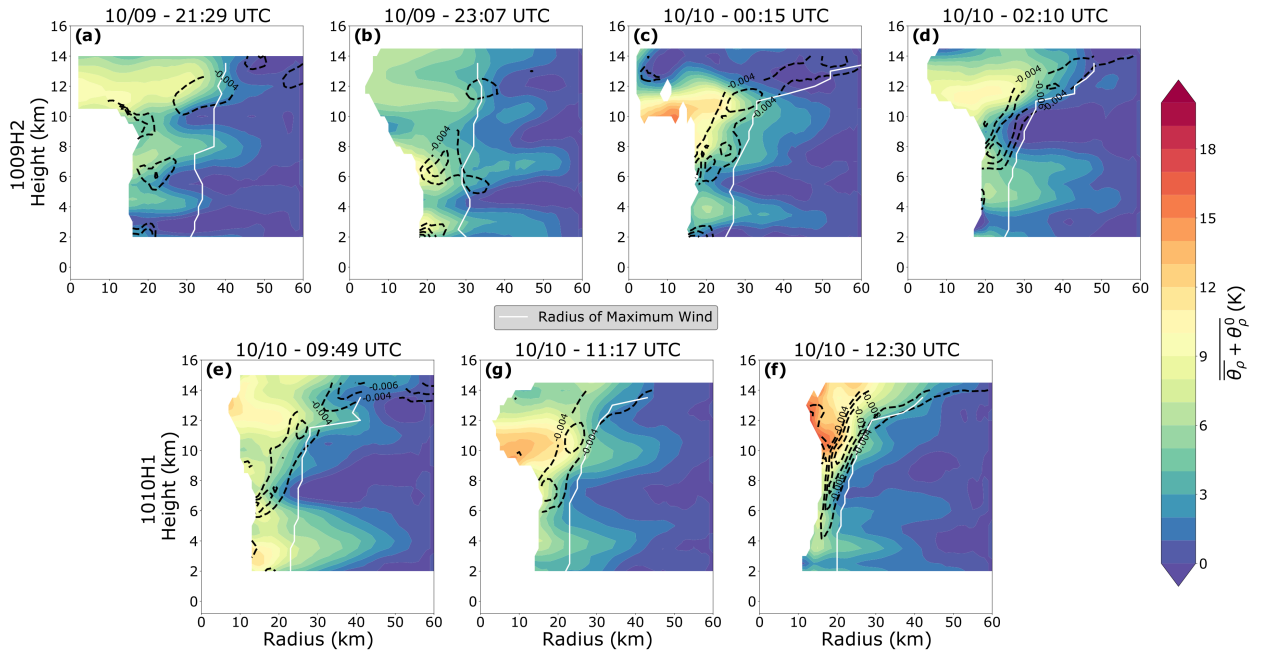


FIG. 10. As in Figure 9 but from aircraft passes at 09:49 UTC (a,d,g), 11:17 UTC (b,e,h), and 12:30 UTC (c,f,i) on 10 October during aircraft mission 1010H1.



826 FIG. 11. Retrieved azimuthally averaged density potential temperature anomalies (color, K) during the last
 827 two aircraft missions, 1009H2 (a,b,c,d) and 1010H1 (e,f,g), prior to landfall. Anomalies are calculated with
 828 respect to the retrieved vertical profile at $r = 60$ km. Contours show the radial gradient of density potential
 829 temperature in K km^{-1} . Analysis times are given above each panel.

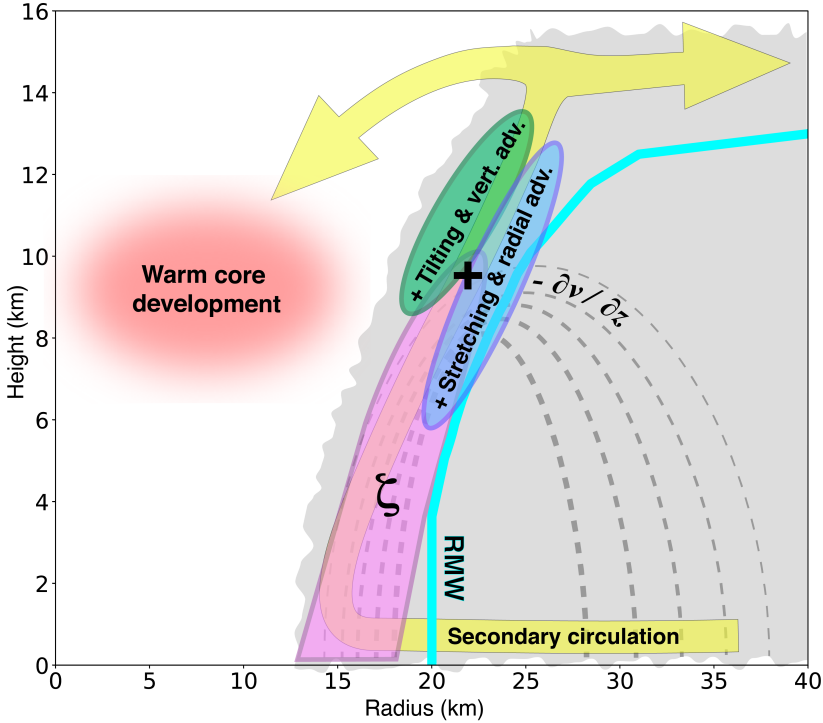


FIG. 12. Schematic representation of observed vortex development processes during rapid intensification of Hurricane Michael (2018). Light gray shading denotes the eyewall cloud. Purple shaded region represents the tower of high vorticity in the eyewall. Green shading denotes region of positive vorticity tendency from tilting and vertical advection. Blue shading represents region of positive vorticity tendency from stretching and radial advection. The + sign denotes the location of the maximized positive net vertical vorticity tendency from the sum of these terms and negative tendencies (not shown). Yellow shading denotes secondary circulation. Cyan contour denotes the radius of maximum wind. Dashed gray contours denote tangential wind, with decreasing line thickness indicating weaker winds. The region of enhanced horizontal vorticity is denoted near 9 km altitude at the same level as the red shaded area where warm core development is maximized through thermal wind balance.